JQS **Journal of Quaternary Science** **QRA**

Climate, glacial and vegetation history of the polar Ural Mountains since *c.* 27 cal ka BP, inferred from a 54 m long sediment core from Lake Bolshoye Shchuchye

MARLENE M. LENZ,[1] ANDREI ANDREEV,[1,2,3] LARISA NAZAROVA,[2,3,4] LIUDMILA S. SYRYKH,[3,5] STEPHANIE SCHEIDT,[1] HAFLIDI HAFLIDASON,[6,7] HANNO MEYER,[2] DOMINIK BRILL,[8] BERND WAGNER,[1] RAPHAEL GROMIG,[1] MATTHIAS LENZ,[1] CHRISTIAN ROLF,[9] GERHARD KUHN,[10] GRIGORIY FEDOROV,[11,12] JOHN INGE SVENDSEN[6,7] and MARTIN MELLES[1]

[1]University of Cologne, Institute of Geology and Mineralogy, Cologne, Germany
[2]Alfred Wegener Institute Helmholtz Center for Polar and Marine Research, Potsdam, Germany
[3]Kazan Federal University, Kazan, Russia
[4]Potsdam University, Institute of Earth and Environmental Science, Potsdam, Germany
[5]Herzen State Pedagogical University of Russia, St. Petersburg, Russia
[6]University of Bergen, Department of Earth Science, Bergen, Norway
[7]Bjerknes Centre for Climate Research, Bergen, Norway
[8]Institute of Geography, University of Cologne, Cologne, Germany
[9]Leibniz Institute for Applied Geophysics (LIAG), Hannover, Germany
[10]Alfred Wegener Institute Helmholtz Center for Polar and Marine Research, Bremerhaven, Germany
[11]St. Petersburg State University, St. Petersburg, Russia
[12]Arctic and Antarctic Research Institute, St. Petersburg, Russia

ABSTRACT: Because continuous and high-resolution records are scarce in the polar Urals, a multiproxy study was carried out on a 54 m long sediment succession (Co1321) from Lake Bolshoye Shchuchye. The sedimentological, geochemical, pollen and chironomid data suggest that glaciers occupied the lake's catchment during the cold and dry MIS 2 and document a change in ice extent around 23.5–18 cal ka BP. Subsequently, meltwater input, sediment supply and erosional activity decreased as local glaciers progressively melted. The vegetation around the lake comprised open, herb and grass-dominated tundra-steppe until the Bølling-Allerød, but shows a distinct change to probably moister conditions around 17–16 cal ka BP. Local glaciers completely disappeared during the Bølling-Allerød, when summer air temperatures were similar to today and low shrub tundra became established. The Younger Dryas is confined by distinct shifts in the pollen and chironomid records pointing to drier conditions. The Holocene is characterised by a denser vegetation cover, stabilised soil conditions and decreased minerogenic input, especially during the local thermal maximum between *c.* 10 and 5 cal ka BP. Subsequently, present-day vegetation developed and summer air temperatures decreased to modern, except for two intervals, which may represent the Little Ice Age and Medieval Warm Period. © 2021 John Wiley & Sons, Ltd.

KEYWORDS: Arctic Russia; chironomids; polar Ural Mountains; pollen; sediment core data

INTRODUCTION

The last time the polar Ural Mountains (north of 65°40′N; Astakhov, 2018) were fully ice-covered probably dates back to Marine Isotope Stage (MIS) 6 (*c.* 160–140 ka BP; Svendsen *et al.*, 2004). Later, during MIS 5d–4, the Barents-Kara Ice Sheet (BKIS) only reached the northern rim of the continent (Svendsen *et al.*, 2004, 2014), causing large ice-dammed lakes on the lowlands on both sides of the Ural Mountains (Mangerud *et al.*, 2004; Svendsen *et al.*, 2014). During the MIS 4 glacial maximum (*c.* 60–50 ka BP), the BKIS presumably merged with outlet glaciers from the mountain range (Fig. 1A). Only small local glaciers existed in the polar Ural Mountains during the Last Glacial Maximum (LGM; 26.5–19 ka BP; Clark *et al.*, 2009), when a very dry climate and strong westerly winds restricted snow accumulation (Mangerud *et al.*, 2008). Thus, in some lake basins in the polar Urals one would expect to find continuous sedimentary archives spanning the LGM period and the time before.

However, most of the archives investigated so far have a limited age range and temporal resolution (e.g. Andreev *et al.*, 2005; Astakhov and Nazarov, 2010 and references therein). Only a few records cover the LGM and earlier periods (e.g. Paus *et al.*, 2003; Henriksen *et al.*, 2008; Svendsen *et al.*, 2014). Particularly promising to provide continuous insight into the Late Quaternary climate, environmental and glacial history of this Arctic region is the sediment record of Lake Bolshoye Shchuchye, the largest and deepest lake in the polar Urals (Fig. 1). Geomorphological fieldwork combined with terrestrial cosmogenic nuclide exposure ([10]Be) and optically stimulated luminescence (OSL) dating suggest that the lake and adjacent areas were covered by a rather large glacier during most of MIS 4 (75–65 ka; Svendsen *et al.*, 2019). A seismic survey showed that the lake basin contains up to 160 m of stratified lacustrine sediments, which formed after the last deglaciation (Haflidason *et al.*, 2019). Additionally, the 23.8 m long core PG506-48/50 was recovered from the very southern part of the lake and studied based on sedimentological and geochemical analyses, pollen, spores and sedimentary ancient
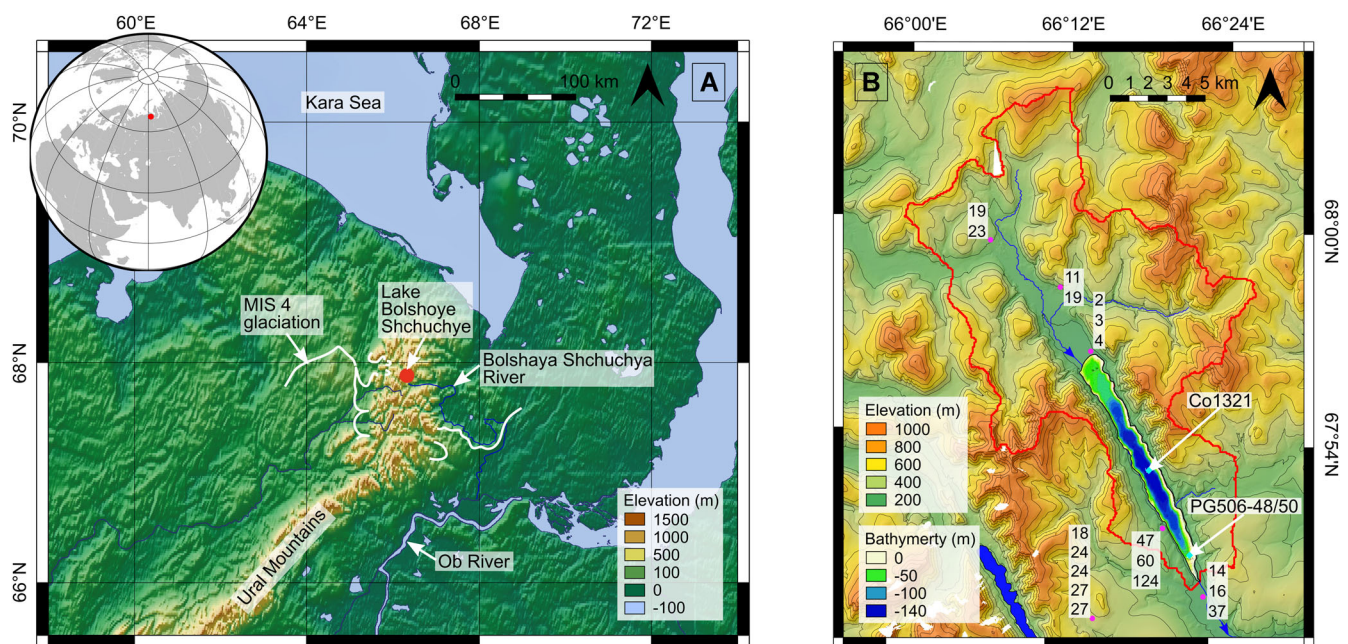
Figure 1. Maps of the study area. 1A. Topographic map of north-western Russia. The location of Lake Bolshoye Shchuchye in the northern polar Urals is marked with a red dot. Some of the most distinct moraines that are presumably from the MIS 4 glaciation are marked with white lines (from Svendsen *et al.*, 2014). The area lies outside the maximum extent of the MIS 2 glaciation. 1B. Topographic map of the catchment of Lake Bolshoye Shchuchye (red line), its bathymetry (Haflidason *et al.*, 2019), the location of core Co1321 (PLOT project) and the composite core PG506-48/50 (CHASE project). Pink dots and associated numbers mark OSL- and [10]Be dating sites with rounded ages (ka) according to Svendsen *et al.* (2019). [Color figure can be viewed at wileyonlinelibrary.com].

DNA and leaf wax hydrogen isotopes (Regnéll *et al.*, 2019; Clarke *et al.*, 2020; Bjune *et al.*, this issue; Cowling *et al.*, this issue). This core is considered to cover the last 23.8 cal ka BP without any hiatuses (Fig. 1). Based on the seismic data and the findings from core PG506-48/50, it was speculated that the entire sediment succession of Lake Bolshoye Shchuchye could reflect the climatic and environmental history during at least the last *c.* 60–50 ka (Haflidason *et al.*, 2019).

In order to expand the existing sedimentological record, Lake Bolshoye Shchuchye was revisited in April 2016 within the scope of the Russian–German research project PLOT (Paleolimnological Transect). During this expedition, a 54 m long sediment succession (Co1321) was recovered from the central part of the lake (Fig. 1). The multidisciplinary investigation of Co1321 intends to expand the knowledge of the local glaciation history beyond 23.8 cal ka BP and to reconstruct the lake development since early MIS 2 times in more detail. This reconstruction includes qualitative and quantitative changes in, for example, terrestrial input, in-lake and catchment productivity, lake-ice cover, precipitation and summer air temperature. For this purpose, a robust age–depth model was generated for the sediment succession using radiocarbon (^{14}C) and OSL ages, as well as palaeomagnetic, palynological and seismo-stratigraphic information.

STUDY AREA

Lake Bolshoye Shchuchye is located at ~187 m above sea level (a.s.l.) and ~150 km north of the Arctic Circle in the central part of the polar Urals (Fig. 1). The lake is up to ~1 km wide and 13 km long and has a maximum water depth of ~140 m in the centre of the lake basin (Haflidason *et al.*, 2019). The lake is surrounded by 500–1000 m high mountains, which steeply decline towards the central and northern part of the lake. The lake catchment comprises about 215 km² and is much larger in the northern than the southern part (Fig. 1). The major inflow, the Pyryantanyë River, enters the lake in the north,

while the Bolshaya Shchuchya River drains the lake in the south into the Ob River and finally into the Kara Sea.

Lake Bolshoye Shchuchye is located in a north-west to south-east striking valley of tectonic origin, which presumably developed during the Uralian Orogeny in the Late Palaeozoic 250–300 Ma ago (Puchkov, 1997), and later became glacially reshaped. The bedrock to the north and east of the lake predominantly consists of Proterozoic to Cambrian basaltic and andesitic rocks, whereas mostly carbonate-bearing sandstones and shales of Ordovician age crop out to the west and south (Fig. 2; Dushin *et al.*, 2009).

Lake Bolshoye Shchuchye today is a cold-monomictic, ultra-oligotrophic lake with complete mixing in summer, when the lake is ice-free for about 3 months. A water temperature profile from April 2016, recorded at the deepest part of the lake, showed an inverse temperature gradient, from 1.2 °C below the 1.5 m thick ice cover to 3.1 °C at the lake bottom (Regnéll *et al.*, 2019). The annual runoff from the catchment area is calculated to ~0.13–0.15 km³ a⁻¹, which implies that the water body can be completely renewed within 5–7 years (Haflidason *et al.*, 2019).

The climate in the area is cold, dry and windy. Mean July and January air temperatures amount to 10.7 °C and -26.9 °C, respectively (New *et al.*, 2002). Mean annual precipitation is around 380 mm, with maximum precipitation occurring in summer (New *et al.*, 2002). The modern-day growing season probably lasts from June to September, when monthly temperatures are above freezing and precipitation is increased. The dominant wind direction is from the west (Svendsen *et al.*, 2019). There are no glaciers in the catchment of Lake Bolshoye Shchuchye today, but small (<1 km²) cirque and hanging glaciers occur in other parts of the polar Urals (Mangerud *et al.*, 2008; Solomina *et al.*, 2010; Svendsen *et al.*, 2019). The lake is located close to the modern northern tree line. Shrub- and herb-dominated tundra communities occupy higher elevations of the catchment, while open larch forests with tree birch and spruce occupy the valley of the Bolshaya Shchuchya River.
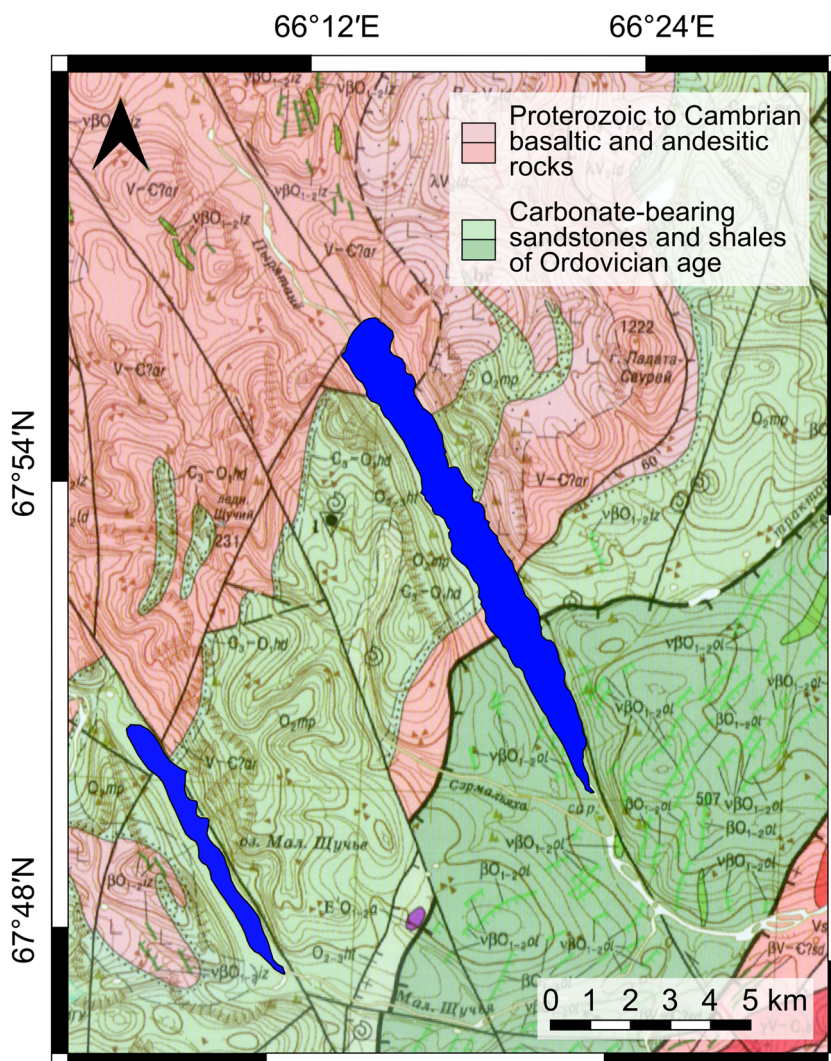
Figure 2. Geological map of the study area modified after Dushin *et al.* (2009), with Lake Bolshoye Shchuchye (centre) and Lake Maloye Shchuchye (bottom left) marked in blue. [Color figure can be viewed at wileyonlinelibrary.com].

MATERIAL AND METHODS

Coring

Sediment coring at Lake Bolshoye Shchuchye was carried out in spring 2016 at 136 m water depth in the central, deepest part of the lake (67°52.8′ N, 66°18.0′ E; Fig. 1), where seismic data indicate up to 160 m thick, acoustically laminated sediments (Haflidason *et al.*, 2019). Coring at site Co1321 was conducted using gravity and percussion piston corers (UWITEC Ltd, Austria) from the ice-covered lake surface. The gravity corer was employed to sample the sediment–water interface and the uppermost 0.84 m below lake floor (b.l.f.). Deeper sediments were recovered with the piston corer with 2 m long core barrel and inner PVC liner. The piston corer was operated in two adjacent holes, penetrating sediments from the lake floor to 15.5 m b.l.f. and between 14 and 54 m b.l.f., respectively. The cores were cut into up to 1 m long segments directly after retrieval and kept dark and stored at ~4 °C during transport to, and while being stored at, the University of Cologne.

Sedimentological, geochemical and magnetic analyses

In the laboratory, the cores were split lengthwise and described for colour, grain size, structure and carbonate content. X-ray fluorescence (XRF) scanning was performed on one core half at 1 mm resolution using an ITRAX core scanner (Cox Analytical, Sweden). The scanner was equipped with a chromium (Cr) X-ray source and a Si-drift detector in combination with a multichannel analyser. Amperage, voltage and exposure time were set to 30 mA, 30 kV and 10 s, respectively. Results are given in total counts per second (cps). Data processing was carried out with the QSpec 6.5 software (Cox Analytical, Sweden). Outliers at the top and bottom of each core and around small cracks in the core segments were excluded from the dataset. For the differentiation and counting of graded laminae in five core sections (~25–26, 33–34, 40–41, 47–48 and 51–52 m b.l.f.), additional high-resolution XRF scanning was performed at 200 μm resolution, 30 mA, 55 kV and an integration time of 5 s. The individual laminae were detected by the ratios of Fe/Si and K/Si and high-resolution linescan images (Regnéll *et al.*, 2019).

Half-core measurements were also conducted for magnetic properties. Magnetic susceptibility (MS) was determined in 1 cm resolution using a multi-sensor core logger (GEOTEK Co., UK) equipped with a Bartington MS2E sensor. Subsequently, measurements of the natural remnant magnetisation were performed, followed by three equally sized alternating field demagnetisation steps of up to 15 mT. Measurements of the remnant magnetisation were carried out in 1 cm spacing using the model 760 cryogenic magnetometer (2-G Enterprise, USA) with an integrated degaussing system (Rolf, 2000) at the rock- and palaeomagnetic laboratory Grubenhagen of the Leibniz Institute for Applied Geophysics (LIAG, Hannover, Germany). The 15 mT demagnetisation step is used to approximate the characteristic remnant magnetisation. The dataset was cleaned for artificial directions that occurred as a result of coring as

well as cutting of the cores into core segments. Additional mineral magnetic evaluation is described in the supplement.

For further analysis, discrete samples (cylindrical plastic vials; diameter = 0.9 cm, height = 4 cm, volume = 2.5 cm^3) were collected from one core half every 8 cm. Sampling at 8 cm offers a temporal resolution of about 50 years between two samples. The material was freeze-dried and the water content was calculated from the mass difference between the wet and dry samples, expressed as weight percentages (wt %) of the original wet sediment sample. Sample aliquots of 0.5 g were homogenised and ground to <63 μm. Total nitrogen (TN) and total sulphur content was quantified by combusting the material in small tin capsules at 1150 °C using a vario MICRO cube elemental analyser (Elementar Corp., Germany). Total carbon (TC) and total inorganic carbon (TIC) content was measured with a DIMATOC 2000 carbon analyser (Dimatec Corp., Germany), with TC determined after combusting the sample material at 900 °C and TIC determined on material pretreated with phosphoric acid (H_3PO_4) and combusted at 160 °C. Total organic carbon (TOC) content was calculated as the difference between TC and TIC. TOC/TN ratios were calculated based on the atomic weights of carbon and nitrogen (Meyers and Teranes, 2001).

Subsamples taken in 16 cm intervals, comprising 2 cm thick sediment slices, were analysed for grain-size distribution, stable organic carbon isotope ratios ($\delta^{13}C_{org}$) and biogenic opal (BO) concentrations. Grain-size analyses were carried out using an LS 13 320 laser diffraction particle size analyzer (Beckman Coulter, Germany). The sample was pretreated with 10% hydrochloric acid (HCl), 35% hydrogen peroxide (H_2O_2) and 1 M sodium hydroxide (NaOH), in order to remove carbonate, organic matter (OM) and biogenic silica, respectively, and finally with sodium pyrophosphate ($Na_4P_2O_7$; Graham's Salt) for sample dispersion. Data processing was carried out using the GRADISTAD v.8.0 software (Blott and Pye, 2001). Grain-size results are given as volume percentage (%) of the particle-diameter classes.

To analyse the carbon isotopic composition, a sample aliquot of ~0.5 g was homogenised and removed of TIC by HCl treatment. The residual material was weighed into tin capsules and combusted at 1020 °C in a ThermoFisher Scientific Delta-V-Advantage gas-mass spectrometer equipped with a FLASH elemental analyser EA 2000 and a CONFLO IV gas-mixing system and an MA200R autosampler system at the Alfred Wegener Institute Helmholtz Centre for Polar and Marine Research (AWI) in Potsdam, Germany. The $\delta^{13}C$ ratios were determined relative to laboratory standards of known isotopic composition and are reported as delta values relative to the VPDB standard in per mil (‰) notation. The standard deviation is generally lower than ±0.15‰.

For the measurement of BO concentrations, sample aliquots of 0.45 g dry sediment were homogenised with a vibration mill. The samples were measured for biogenic silica (BSi) according to the automated sequential leaching method (Müller and Schneider, 1993) at the AWI in Bremerhaven, Germany. BO was calculated from BSi assuming 10% water content within the frustules (Mortlock and Froelich, 1989; Müller and Schneider, 1993).

Palaeoecological analyses

Pollen analyses were carried out on 83 horizons sampled with cylindrical plastic vials (diameter = 0.9 cm, height = 4 cm, volume = 2.5 cm^3). The distance between the samples is on average 42 cm in the upper 13.5 m of core Co1321 and 80 cm below. With respect to changing sedimentation rates, the 83 samples account for an average temporal resolution of about

330 years between two samples. A standard high-frequency technique (Berglund and Ralska-Jasiewiczowa, 1986) was used for sample preparation. A tablet of *Lycopodium* marker spores (20 848 spores per tablet) was added to each sample to calculate the total pollen and spore concentration following Stockmarr (1971). Water-free glycerol was used for sample storage and for preparation of microscopic slides. Pollen identification was done at magnification 400 with the aid of published pollen keys and atlases (Kupriyanova and Alyoshina, 1972; Kupriyanova and Alyoshina, 1978; Bobrov *et al.*, 1983; Reille, 1992, 1995, 1998). At least 250 pollen grains were counted in each sample. The relatively low number is determined by the scarcity of pollen grains in samples from the Arctic. Counting at least 200–250 pollen grains, however, has proven to be suitable to obtain reliable results in previous work in the Russian Arctic (e.g. Andreev *et al.*, 2005, 2011, 2012). In addition to pollen, spores, remains of algae, spores of fungi and other non-pollen palynomorphs (NPP) were counted (van Geel, 2002 and references therein). The sediments in the lower part of the core also contain large amounts of redeposited pre-Quaternary pollen and spores, which are distinguishable by darker colour, poor preservation and exotic taxa other than the Quaternary ones. The relative abundance of the pollen taxa was calculated from the sum of the terrestrial pollen taxa. The percentages of spores are based on the sum of pollen and spores. The percentages of algae are based on the sum of pollen and algae, and the percentages of fungi spores are based on the sum of pollen and fungi spores. The relative abundance of redeposited, pre-Quaternary pollen and spores was calculated based on the sum of pollen and redeposited taxa. The TGView software (Grimm, 2004) was used to calculate percentages. Pollen zones were assigned by qualitative inspection of significant changes in the pollen assemblages, the pollen concentrations and the occurrence of particularly indicative taxa.

Seventy-three sediment samples (~2 g sample aliquot of selected 2 cm thick sediment slices) were prepared for chironomid analyses. The distance between the samples is on average 32 cm in the upper 13.5 m of core Co1321 and 128 cm below. With respect to changing sedimentation rates, the 73 chironomid samples offer an average temporal resolution of ~380 years between two samples. Pretreatment of the samples followed standard techniques described by Brooks *et al.* (2007). Chironomids were identified to the highest possible taxonomic resolution with reference to Wiederholm (1983) and Brooks *et al.* (2007). Information on the ecology of chironomid taxa was taken from Brooks *et al.* (2007), Moller Pillot (2009) and Nazarova *et al.* (2008, 2011, 2015a, 2017a,b). Several studies have demonstrated that a sample size of 50 head capsules is adequate for a reliable estimate of inferred air temperature (Heiri and Lotter, 2001; Larocque, 2001; Quinlan and Smol, 2001). To better constrain the diversity of the chironomid population, adjacent samples were merged, when necessary (CZ VII and V), to obtain at least 50 chironomid remains. Because only a few sediment samples below 40 m core depth included chironomid remains, samples from this depth interval could not be reasonably merged. Therefore, the reconstruction of mean July air temperatures (T_{July}) was only performed for the upper 40 m of the sediment succession. T_{July} was reconstructed using the North Russian (NR) chironomid-based temperature inference model (WA-PLS, 2 component; r2 boot = 0.81; RMSEP boot = 1.43 °C), which is based on the modern calibration dataset of 193 lakes and 162 taxa from northern Russia (61–75°N, 50–140°E, T_{July} range 1.8–18.8 °C) published by Nazarova *et al.* (2015a). The RMSEP (root mean squared

error of prediction) boot parameter indicates that the average error of the temperature reconstruction using this model is 1.43 °C. The T_{July} NR model was previously applied for palaeoclimatic inferences in Siberia and the European part of northern Russia and demonstrated high reliability of the reconstructed parameters (Nazarova *et al.*, 2017b, 2020; Syrykh *et al.*, 2017; Wetterich *et al.*, 2018).

Chronostratigraphical analyses

To extract plant fragments for ^{14}C dating, the >63 µm fraction was isolated by sieving and density-separation with a sodium polytungstate solution (3 Na_2WO_4, 9 WO_3, H_2O) calibrated to 2.5 g cm^{-3}. Most plant fragments were too small for taxa identification and may include terrestrial and aquatic remains. Thirteen samples of plant remains were measured at the Centre for Accelerator Mass Spectrometry (AMS) of the University of Cologne (CologneAMS; Dewald *et al.*, 2013; Table 1). Sample pretreatment and graphitisation followed the standard protocol by Rethemeyer *et al.* (2013). An additional two samples of plant macrofossils were prepared by acid-alkali-acid treatment, graphitised and subsequently radiocarbon-dated at the AWI in Bremerhaven. ^{14}C dating of bulk sediment material was carried out on 13 samples at the BETA Analytic Radiocarbon Dating Laboratory (Miami, Florida, USA) after pretreatment with acid washes according to the standard beta analytic protocol. Three further samples of bulk sediment material were

decarbonated with HCl, graphitised and measured at the AWI in Bremerhaven.

OSL dating was carried out on five samples from 9.4, 23.8, 27.8, 52.0 and 54.0 m core depth (Table 2). In order to avoid light exposure, some samples were already taken in the field from core catcher material, which was transferred into opaque PVC tubes immediately after core recovery. Additional samples were taken later in the laboratory from the central part of intact 10 cm core sections. Dating was performed at the Cologne Luminescence Laboratory using fine-grained quartz (all samples) and polymineral fine grains (samples OSL29 and OSL30; Table 2). Samples for burial-dose determination were taken from core sections opened under subdued red light and pretreated following standard procedures to extract the 4–11 µm quartz and polymineral fraction (e.g. Zander and Hilgers, 2013). Samples were pipetted onto 9.8 mm steel discs and measured on a Risø TL/OSL reader with a $^{90}Sr/^{90}Y$ beta source delivering ~0.12 Gy s^{-1} at the sample position. OSL signals were stimulated by means of blue LEDs (quartz) or infrared LEDs (feldspar in polymineral samples) and detected through Hoya U340 (quartz) or interference (feldspar) filters. Quartz equivalent dose measurements followed the SAR protocol of Murray and Wintle (2003) with 10 s preheat at 220 °C and a cut heat at 200 °C. Dose determination for feldspar was based on a post-infrared-infrared (pIRIR) protocol with a post-IR temperature of 225 °C (pIRIR$_{225}$, Thomsen *et al.*, 2008).

The appropriateness of the applied protocols was checked by means of preheat tests (preheat plateau for quartz at

Table 1. Radiocarbon data obtained from core Co1321. The dating was performed at the CologneAMS Centre (COL), the BETA Analytical Radiocarbon Dating Laboratory (BETA) and the Alfred Wegener Institute, Helmholtz Centre for Polar and Marine Research in Bremerhaven (AWI). The sample material consisted of either plant macrofossils (pm) or bulk sediment (bs). Ages used for the age–depth model are marked in bold. Ages originating from intervals considered as artificially relocated material from the upper part of the record due to malfunctions during coring are indicated with 'ar'. Ages were calibrated with CLAM version 2.3.9 in R (Blaauw, 2010. 2021; R Core Team, 2020)

Sample ID	Composite depth (m c.d.)	Material	Mass C (µg)	Uncalibrated ^{14}C age (a BP)	Calender age (cal a BP)	Min. (cal a BP)	Max. (cal a BP)
COL4879	**0.95**	**pm**	**503**	**1718 ± 46**	**1591**	**1533**	**1708**
AWI5283	1.88	bs	884	3126 ± 18	3363	3259	3392
AWI5282	**2.40**	**pm**	**176**	**3712 ± 36**	**4024**	**3929**	**4215**
AWI5284	2.82	bs	441	4989 ± 21	5720	5606	5854
COL4880	**4.95**	**pm**	**320**	**6312 ± 57**	**7255**	**7024**	**7418**
AWI5285	**5.26**	**pm**	**187**	**6276 ± 54**	**7245**	**7014**	**7313**
AWI5286	6.68	bs	453	8523 ± 31	9530	9482	9541
COL4881	**8.52**	**pm**	**993**	**9530 ± 50**	**10 980**	**10 663**	**11 092**
COL5252	**12.64**	**pm**	**478**	**12 765 ± 75**	**15 230**	**15 009**	**15 496**
BETA478505	13.15	bs		14 860 ± 40	18 210	18 101	18 268
COL4882	**15.20**	**pm**	**995**	**13 563 ± 65**	**16 350**	**16 169**	**16 589**
BETA478506	17.42	bs		18 680 ± 60	22 520	22 417	22 870
BETA478507	20.76	bs		20 160 ± 60	24 170	23 939	24 442
COL4883	**22.42**	**pm**	**318**	**14 003 ± 86**	**17 040**	**16 752**	**17 335**
COL4887	22.67	bs		22 040 ± 119	26 320	25 942	26 733
COL5253	26.03	pm, ar	996	5418 ± 45	6240	6013	6301
COL4888	30.07	bs		25 219 ± 149	29 300	29 181	29 897
COL5254	34.60	pm, ar	176	4530 ± 105	5290	4873	5463
BETA478508	34.73	bs		24 510 ± 90	28 760	28 587	29 037
COL4884	37.20	pm, ar	998	4071 ± 41	4562	4423	4804
BETA478509	38.91	bs		25 820 ± 100	30 060	29 946	30 261
BETA478510	41.59	bs		26 430 ± 120	30 820	30 355	31 002
COL4885	**43.02**	**pm**	**367**	**17 154 ± 112**	**20 760**	**20 476**	**20 931**
COL4886	44.74	pm, ar	717	4391 ± 42	4964	4854	5265
COL4889	44.81	bs, ar		9593 ± 55	11 070	10 747	11 167
COL4890	45.79	bs		29 800 ± 221	34 340	33 909	34 656
COL5255	**49.85**	**pm**	**822**	**18 609 ± 95**	**22 480**	**22 352**	**22 865**
BETA478511	49.91	bs		23 030 ± 90	27 300	27 184	27 566
BETA478512	52.88	bs		26 020 ± 110	30 200	30 016	30 712
COL5256	**53.64**	**pm**	**427**	**24 089 ± 179**	**28 260**	**27 837**	**28 671**
BETA478513	53.78	bs		25 830 ± 110	30 080	29 946	30 285

Table 2. Summary of the optically stimulated luminescence data obtained from core Co1321. N – number of aliquots, Dose – burial dose

Sample ID	Composite depth (m c.d.)	Mineral	N	Dose (Gy)	Water (%)	Dose rate (Gy ka^{-1})	Age (ka)
C-L4232	9.39	quartz	10	33.6 ± 0.6	49 ± 10	3.2 ± 0.2	10.3 ± 0.7
C-L4212	23.53	quartz	12	48.3 ± 0.5	34 ± 10	2.9 ± 0.2	16.6 ± 1.2
C-L4214	27.59	quartz	12	47.3 ± 0.5	39 ± 10	2.9 ± 0.2	16.1 ± 1.1
C-L4226	51.78	quartz	18	63.6 ± 0.6	31 ± 10	3.0 ± 0.2	21.2 ± 1.5
C-L4226	51.78	feldspar pIRIR$_{225}$	6	69.2 ± 0.8	31 ± 10	3.7 ± 0.3	19.6 ± 1.7
C-L4227	53.85	quartz	10	64.3 ± 1.2	55 ± 10	2.2 ± 0.1	28.9 ± 1.8
C-L4227	53.85	feldspar pIRIR$_{225}$	6	68.4 ± 0.8	55 ± 10	2.7 ± 0.2	26.7 ± 2.3

180–280 °C), dose recovery tests (mean dose recovery ratios of 1.00 ± 0.02 for quartz and 1.03 ± 0.04 for the feldspar pIRIR signal), residual dose measurements after 24 h of solar simulator bleaching (pIRIR residual doses of less than 3% of the natural dose), and continuous-wave curve-fitting (quartz signals dominated by the fast component). For each sample between 6 and 18 aliquots passed standard SAR acceptance criteria. Since equivalent dose distributions with overdispersion values of less than 5% indicate homogeneous resetting of both quartz and feldspar OSL signals, the burial-dose calculation was based on the central age model (Galbraith et al., 1999). Dose rate and age calculation were performed using the DRAC software (Durcan et al., 2015), whereas the dosimetry was based on radionuclide concentrations (uranium, thorium, potassium) in the surrounding sediment derived from high-resolution gamma spectrometry measured at the VKTA Rossendorf, Germany, internal potassium content of $12.5 \pm 0.5\%$, and in situ water content. Feldspar pIRIR$_{225}$ ages were corrected for signal loss by anomalous fading using the approach of Huntley and Lamothe (2001) and a g-value of $0.6 \pm 0.5\%$ per decade (mean value of the five samples).

The age–depth model for the sediment record at site Co1321 was calculated with the CLAM software package, which uses 'classical' age modelling (version 2.3.9; Blaauw, 2010, 2021) instead of Bayesian age modelling such as performed by Bacon (Blaauw and Christen, 2011), because Bacon would assume abrupt changes of the sedimentation rate at the tie points if no additional variables are defined. CLAM was run using R version 4.0.3 as an interface (R Core Team, 2020) and IntCal20 (Reimer et al., 2020) for calibration of the radiocarbon dates into calendar years before present (1950 AD). The age–depth curve results from the mean value of the error range and was used to calculate the sedimentation rate.

The variability of the radiocarbon reservoir effects of bulk OM has been calculated from the differences between the respective ^{14}C ages of the bulk sediment and the age–depth model.

RESULTS

Core composite and lithology

Overlapping sections of the parallel holes at site Co1321 were obtained between 14.0 and 15.3 m b.l.f. and were correlated based on the core description, MS and XRF element data using the Corewall software package (Corelyzer 2.0.4 National Lacustrine Core Facility LacCore, Continental Scientific Drilling Coordination Office, CSDCO). The resultant core composite has a total length of 53.88 m correlated depth (mcd) but is not complete (Fig. 3). Minor gaps of a few centimetres often occur between succeeding core segments from gas expansion and loss of material at the core ends. Additional gaps of 10 cm result from OSL sampling (see previous chapter). Much larger gaps between 34.86 and 38.11 mcd, 43.57 and 45.13 mcd,

and 48.00 and 49.02 mcd originate from obvious coring artefacts. These intervals are characterised by deformed sedimentary structures, abrupt changes in the chemical, grain-size and pollen data to neighbouring sediments, as well as Late Glacial to mid-Holocene ^{14}C ages. As these characteristics suggest an origin from the upper part of the record, possibly due to premature, inadvertent opening of the core barrels, the respective sediments were excluded from the investigations, resulting in a total sediment recovery of 85.7%.

Core Co1321 consists of fine-grained, distinctly laminated (54–23.5 mcd) to diffusely layered (13–0 mcd) hemipelagic sediments with interbedded event layers (Fig. 3). The transition between 23.5 and 13 mcd appears gradual and is accompanied by a colour change from grey to brown. Each well-defined rhythmite is made up of a couplet of a darker, basal layer of coarser particles grading into an upper layer of more light-coloured, finer particles. These rhythmic laminations have been identified as annually deposited, glacial varves in sediment record PG506-48/50 from the southern part of Lake Bolshoye Shchuchye (Regnéll et al., 2019). The varve count (number of varves per 1 m sediment) in the core sections ~25–26, ~33–34, ~40–41, ~47–48 and 51–52 mcd (Table 3, Fig. 3) suggests that the varve thickness is highest in the core sections ~33–34 and ~40–41 mcd (2.5–9 mm) and lowest in the core section 51–52 mcd (1.6–2.5 mm). The occasionally interbedded event layers of 0.1–38 cm thickness show distinct fining-upward successions. In accordance with Regnéll et al. (2019), they are interpreted as turbidites. From 54 to 13 mcd, the turbidites are, in colour and sedimentological appearance, difficult to distinguish from the varves. Between 9 and 13 mcd, grain-size-specific colour changes become more apparent. In the upper 9 mcd, the turbidites show distinctive colour changes from grey coarse sand or dark brown silt at the bottom over brown or green fine silt to a white or light brown clay at the top. Turbidites thicker than 1 cm, which comprise a cumulative thickness of 9.06 m or 22.5% of core Co1321, have been omitted from sampling intervals and accordingly been taken out of the XRF and susceptibility data, in order to confine the proxy interpretation to the hemipelagic sedimentation in the lake.

Chronostratigraphy

The age–depth model of core Co1321 is based on the surface age (2016, i.e. the year of core recovery), AMS ^{14}C dating, pollen stratigraphy, correlation with well-dated seismic unit boundaries in Lake Bolshoye Shchuchye, as well as palaeomagnetic and OSL dating (Fig. 3). Four ^{14}C dates on plant macrofossils have been excluded from the age modelling, as they are considered to originate from misplaced sediment due to inadvertent coring (see above). The remaining 11 AMS ^{14}C dates on plant remains are assumed to provide reliable ages without a reservoir effect (e.g. Wood, 2015).

An additional three tie points were derived based on changes in the pollen composition in core Co1321 and dating
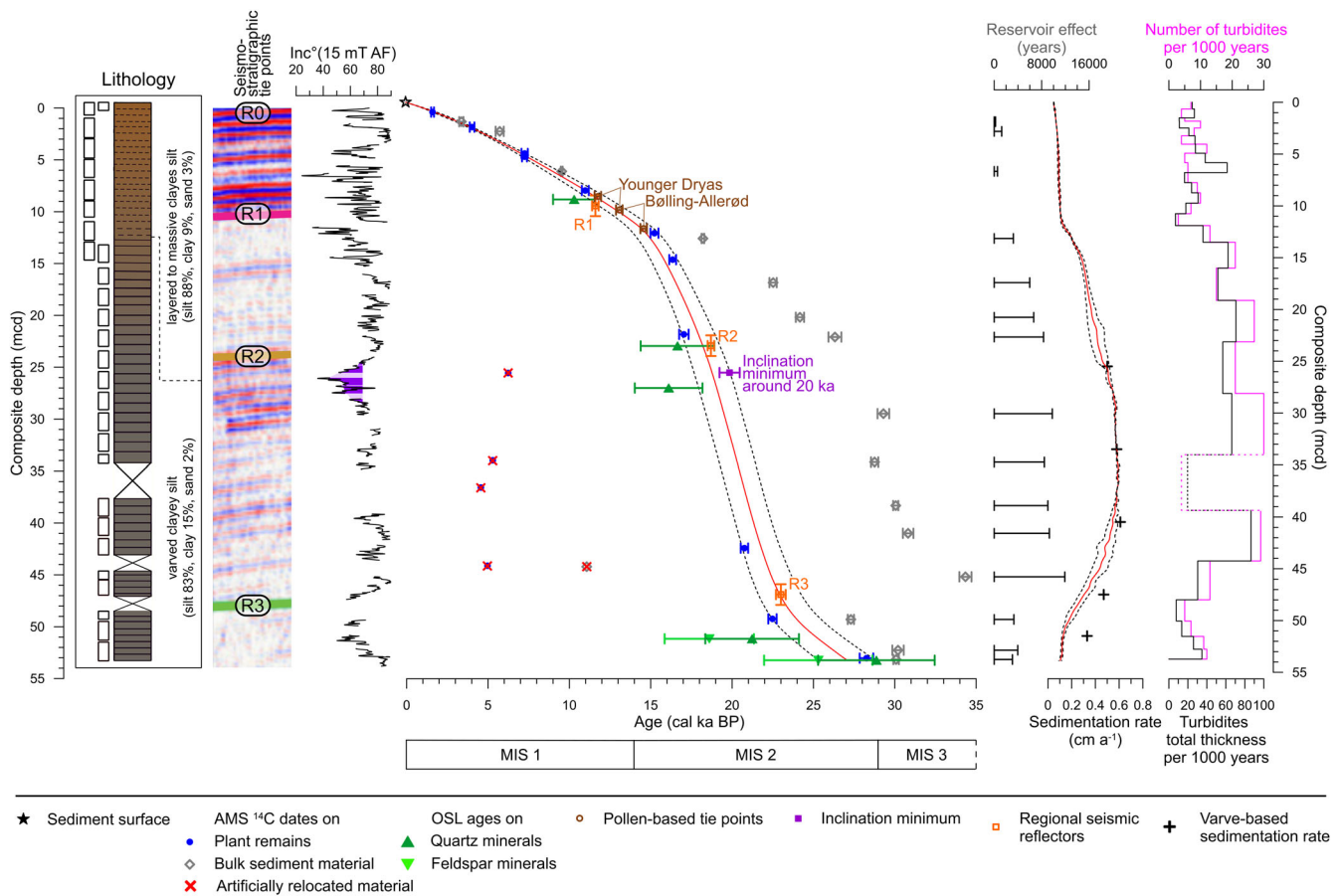
Figure 3. Recovery (open rectangles), variations in sediment lithology and the age–depth model of the 54 m long core Co1321 from the central part of Lake Bolshoye Shchuchye. Ages were calculated using the CLAM 2.3.7 software package in R (Blaauw, 2010, 2021; R Core Team, 2020). The age–depth model is based on the modern sediment surface, eleven ^{14}C AMS dates on plant remains (pm; Table 1), three pollen-zone boundaries, three seismo-stratigraphic tie points modified after Haflidason *et al.* (2019), an inclination minimum following Haflidason *et al.* (this issue). The model is supported by seven OSL dates (Table 2) and varve counting in selected core intervals (Table 3). Four ^{14}C AMS ages on plant remains and one ^{14}C AMS age on bulk sediment material have been omitted, because they apparently originate from artificially relocated material from the upper part of the record due to malfunctions during coring (labelled 'ar' in Table 1). The ^{14}C AMS ages on bulk sediment material indicate a reservoir effect (grey bars), which is highest during times of elevated sedimentation rate. Changes in the sedimentation rate derived from the age–depth model are at least partly controlled by the number and accumulative thickness of turbidites. [Color figure can be viewed at wileyonlinelibrary.com].

Table 3. Results of the varve count (varves per 1 m sediment and inferred sedimentation rate) on five core sections from the lower 25 mcd of core Co1321

Depth interval (m c.d.)	Varves per 1 m	Inferred sedimentation rate (cm a^{-1})
~25–26	201	~0.5
~33–34	173	~0.58
~40–41	164	~0.61
~47–48	213	~0.47
~51–52	295	~0.33

of respective changes in core PG506-48 (Fig. 3; Bjune *et al.*, this issue).

The age model further includes the depth and age information from the three regional seismic reflectors at site Co1321, R1, R2 and R3, which are based on chronological constraints from cores PG506-48/50 (Svendsen *et al.*, 2019). The depths of the seismic reflectors in core Co1321 are slightly modified compared with Haflidason *et al.* (2019) according to the latest seismic interpretation. The seismic tie points may be subject to relatively large depth and age uncertainties, because the vertical resolution of seismic data is limited to several decimetres, the basin-wide tracking of the seismic reflectors is

difficult in some parts and/or age inconsistencies may occur in one or both age models.

The prominent inclination minimum at 26.11 mcd (between ~24.5 and 28.5 mcd) is confined to a time interval of around 20 ka based on a very recent study from Lakes Bolshoye and Maloye Shchuchye (Haflidason *et al.*, this issue). The reliability of the age is further supported by the occurrence of excursional behaviour of the Earth's magnetic field reported in a number of studies around the globe (Singer *et al.*, 2014 and references therein; Channell *et al.*, 2018; Reilly *et al.*, 2018). The palaeomagnetic data in Fig. 3 are restricted to the inclination, because the core sections are not azimuthally oriented and the grain-size variations caused by turbidites do not allow for the approximation of the relative palaeointensity from whole core measurements.

Further support for the age–depth model comes from the quartz and feldspar ages, which are within the error range of the model. The fact that the mean ages tend to underestimate the age model could be related to uncertainties in determining the water content, because the loss of water by compaction can only be estimated. The feldspar and quartz ages for samples C-L4226 and C-L4227 (Table 2) are identical within their errors, thus suggesting that the grains were completely bleached.

Due to the age uncertainty of the individual tie points, the age–depth model exhibits relatively large error bars, especially

below the Bølling-Allerød chronozone. The age uncertainty is up to ±1.8 ka in the lowermost part of the core. For the definition of the boundaries of the sediment units, the mean value of the error range was calculated (red line in Fig. 3).

The reservoir effect of the ^{14}C ages obtained from bulk sediment samples is on average 4 ka below ~50 mcd, varies between 8.4 and 11.5 ka from ~39-23 mcd, decreases from 8.3 to 3.2 ka from ~23–13 mcd and is relatively small (≤500 years) above (Fig. 3).

The sedimentation rates derived from the age–depth model have fairly large uncertainties, in particular at ~50-40 and ~25-20 mcd, where the minimum and maximum age–depth estimates differ most. They reflect changes in hemipelagic deposition but are also influenced by the deposition and erosional capacity of turbidites. The average sedimentation rates account for ~0.1 cm a^{-1} until 51.0 mcd, rapidly increase to their highest values of 0.6 cm a^{-1} from 40 to 28 mcd and then gradually decrease to ~0.1 cm a^{-1} from 12 mcd to the sediment surface. These values are well confirmed by the sedimentation rates derived from the varve count on the core sections ~25–26, ~33–34 and ~40–41 (Table 3, Fig. 3). The sedimentation rates from varve analyses in the core sections ~47–48 and 51–52 mcd are significantly higher than the rates derived from the age–depth model, but still support the observation that the deposition rate decreased towards the bottom of the core (Table 3, Fig. 3).

The age–depth model was further used to constrain the occurrence of turbidites thicker than 1 cm in the record, which involves their number and their accumulative thickness per 1000 years (Fig. 3). Both proxies agree very well with the changes in the sedimentation rates from the age–depth model, showing a broad maximum between ~44 and 19 mcd. In this depth interval, 21–30 turbidites of 57–87 cm accumulative thickness occur per 1000 years, except from the depth interval ~34–39 mcd, where a much lower number and thickness can be at least partly attributed to the core gap between 34.86 and 38.11 mcd.

Physical and geochemical proxy data

Based on their physical and geochemical characteristics, the hemipelagic sediments of core Co1321 can be subdivided into five sediment units (SU V–I) of individual composition, which reflect different depositional settings.

In the basal SU V (27.1–23.5 cal ka BP; 53.8–49.0 mcd) the clay content is relatively high (15%), while the amount of the sand fraction is low and variable. MS and Ti increase towards the top of the unit (Fig. 4). TOC anticorrelates with MS and Ti but remains <11%. TIC is partly elevated with higher values in the lower part of the unit. Water content is between 20.7 and 26.1%. BO is overall relatively low, except for a sharp increase from 5 to 10% at the top of SU V. $\delta^{13}C_{org}$ values with an average of -26.3‰ are relatively heavy. TOC/TN are around or less than 10.

In SU IV (23.5–18.2 cal ka BP; 49.0–23.5 mcd) clay and silt content remains relatively constant and on a high level, whereas the sand content is low (Fig. 4). MS, Ti and the water content increase marginally throughout this unit. TIC is strongly fluctuating at slightly increased values. TOC content is around 0.4%, $\delta^{13}C_{org}$ averages at -26.0‰ and BO is around 8%, except for a peak at 19.4 cal ka BP (29.4 mcd). Below ~20.5 cal ka BP (~35 mcd), TOC/TN fluctuates between 5 and 11 and decreases gradually above.

SU III (18.2–14.9 cal ka BP; 23.5–13.0 mcd) displays a steady decrease in clay content, MS and TOC/TN, whereas silt content, Ti and water content increase (Fig. 4). TOC/TN remains <7. TIC highly fluctuates and shows a sudden decline at the top of the unit to negligible values. TOC remains relatively constant at around 0.4%, BO is slightly increased to about 9%, whereas $\delta^{13}C_{org}$ averages at values of -26.1‰ below ~16 cal ka BP (~16 mcd) and decreases to -28.0‰ towards the top of SU III.

In SU II (14.9–11.5 cal ka BP; 13.0–9.0 mcd) the clay content is relatively low (9%). Sand content is relatively low but variable. MS shows a maximum in the lower part of the unit and decreases above ~13.5 cal ka BP (~11 mcd; Fig. 4). Ti is relatively high with maximum values at the top of the unit. TIC is negligible. TOC and water content increase gradually. TOC/TN is highly fluctuating and increases towards the top. Compared with SU III, BO has decreased to around 6% and $\delta^{13}C_{org}$ remains around -28‰.

SU I (11.5–0 cal ka BP; 9.1–0 mcd) sediments have maximal silt content of up to 90%. The sand content is slightly elevated below ~5 cal ka BP (~3 mcd) and shows low values above. MS, Ti and $\delta^{13}C_{org}$ decrease distinctly between ~11.5 and 8 cal ka BP (~9 and 6 mcd) to their overall lowest values, slightly increase above to show relatively stable values in the upper 3 m. Minimum values in $\delta^{13}C_{org}$ are around -34.5‰. Opposite trends are shown by the water content, TOC and BO, although TOC and BO display relatively high variability above ~8 cal ka BP (~6 mcd). TIC is almost absent. TOC/TN increases from 7 to 10 below ~5 cal ka BP (~3 mcd) and shows relatively stable values above.

Pollen, spores and non-pollen palynomorphs

A total of 53 different pollen, spore, and NPP taxa have been found in core Co1321, the most important of which are presented in Fig. 5 along with the total pollen concentration. The pollen assemblages can be subdivided into six main pollen zones (PZ VI–I), which have different boundaries from the sediment units described above (Fig. 5).

PZ VI (27.1–16.3 cal ka BP; 53.8–16.5 mcd) has an overall low pollen concentration and is dominated by pollen of Poaceae, Cyperaceae and *Artemisia*, while pollen of trees and shrubs is rare. The pollen zone shows relatively high amounts of green algae colony remains (*Pediastrum*), spores of *Glomus* and obviously reworked microfossils (such as pre-Quaternary spores and Pinaceae, *Osmunda cinnamomea*, dinoflagelates, *Ilex* and *Tilia* pollen).

PZ V (16.3–14.4 cal ka BP; 16.5–12.2 mcd) is characterised by a moderate pollen concentration with increased content of Cyperaceae and *Salix* pollen. Tree and shrub pollen remains rare, while the percentages of *Artemisia* and Poaceae pollen are persistently high. Amounts of *Glomus* spores are distinctly decreased. Presence of *Pediastrum* remains and pre-Quaternary palynomorphs decreases towards the top of PZ V.

In PZ IV (14.4–12.9 cal ka BP; 12.2–10.4 mcd) the pollen concentration remains moderate, but *Betula* sect. *Nanae* pollen content is strongly increased. The percentages of *Artemisia* pollen are high, while the percentages of Poaceae and Cyperaceae are slightly decreased.

PZ III (12.9–11.5 cal ka BP; 10.4–9.1 mcd) also shows a moderate pollen concentration, but slightly higher content of herb pollen, in particular *Artemisia* and Cyperaceae, and lower content of *Betula* sect. *Nanae*.

In PZ II (11.6–10.7 cal ka BP; 9.1–8.2 mcd) the pollen concentration remains moderate. The PZ displays a maximum in *Betula* sect. *Nanae* and *Salix* pollen percentages and strong decreases in Poaceae, Cyperaceae, *Artemisia* and other herbs.

PZ I (10.7–0 cal ka BP; 8.2–0 mcd) shows the highest pollen concentrations, lowest percentages of herbs (Poaceae, Cyperaceae, *Artemisia)* and a dominance of shrub and tree taxa (in particular *Betula* sect. *Albae* and *Alnus fruticosa*). The zone
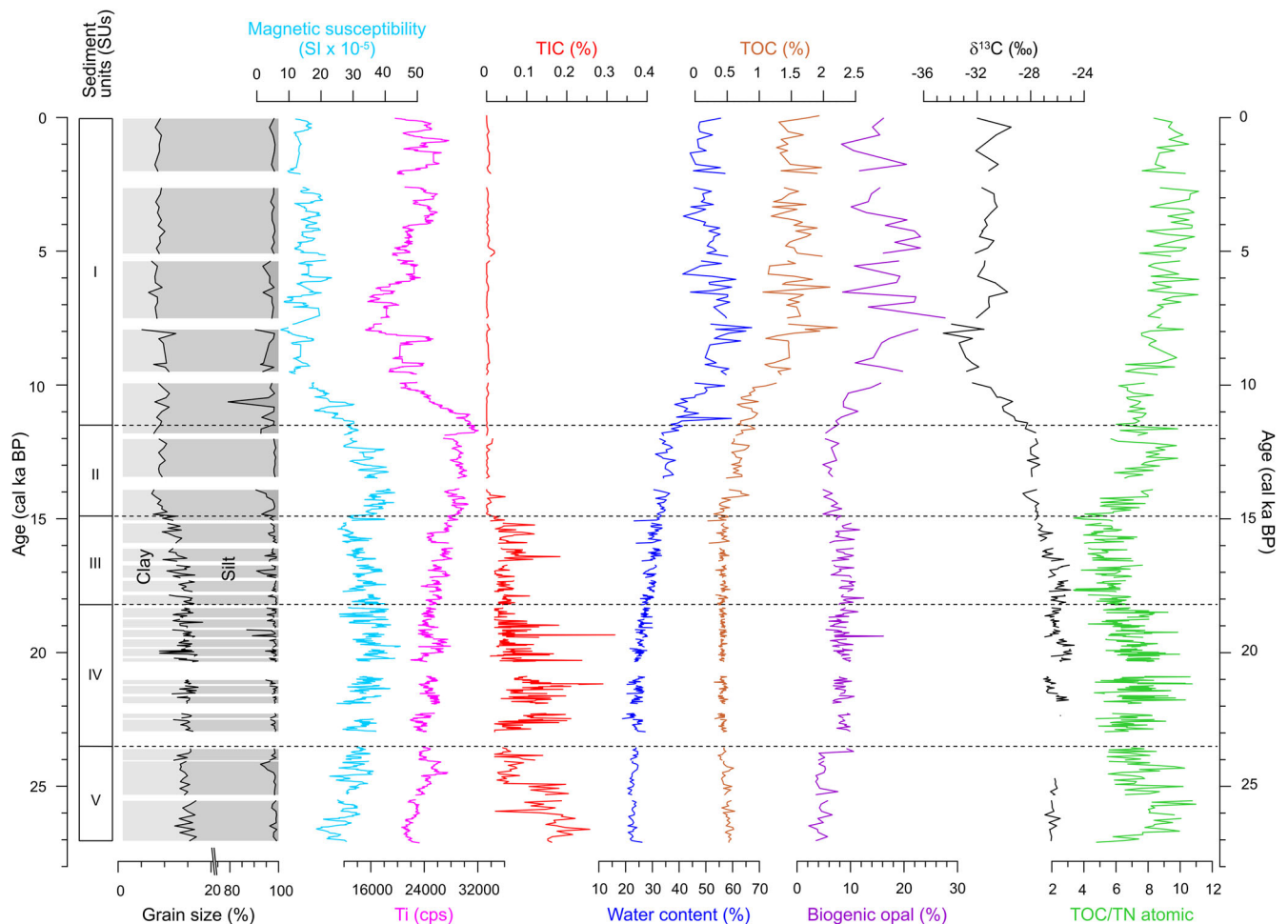
Figure 4. Selected physical and geochemical proxy data of core Co1321 (MS = magnetic susceptibility, TIC = total inorganic carbon, TOC = total organic carbon, TN = total nitrogen) plotted against age. Based on these data, the hemipelagic sediments were subdivided into five sediment units (SU I–V) of individual composition. High-resolution XRF and MS data are smoothed by 81-point and 9-point running averages, respectively. [Color figure can be viewed at wileyonlinelibrary.com].

can be subdivided into two subzones, with PZ Ib (10.7–4.7 cal ka BP; 8.2–3.0 mcd) characterised by higher pollen concentration and a higher presence of *Alnus fruticosa* pollen than PZ Ia.

Chironomids

A total of 75 chironomid taxa were identified in core Co1321. The fauna is dominated by two taxa from the genus *Heterotrissocladius*: *H. subpilosus*-type and *H. grimschawi*-type (Fig. 6). Seven chironomid zones (CZ VII–I) can be differentiated in core Co1321. Two zones (CZ VII and V) contained relatively low concentrations of chironomid remains. The data for these zones, including the temperature reconstructions, therefore have to be treated with caution.

CZ VII (27.1–19.8 cal ka BP; 53.8–32 mcd) is based on only a few samples from the lower part of the core, which contain head capsules of chironomids. The fauna is composed of the taxa *H. subpilosus*-type, *Hydrobaenus lugubris*-type and *Orthocladius* type S. The sum of lotic taxa (e.g. *Metriocnemus*, *Thienemanniella clavicornis*-type, *Diamesinae* sp.) is occasionally high. At 21.5 cal ka BP (41.7 mcd) *Trissocladius* appears in the fauna. *Smittia-Parasmittia* occurs at 20.2 cal ka BP (34 mcd). The temperature reconstruction points to it being 1.5 °C lower than the modern T_{July} of 10.7 °C.

In CZ VI (19.8–15.3 cal ka BP; 32–13.9 mcd) the chironomid diversity increases and the taxon *Hydrobaenus lugubris*-type is abundant. The total amount of lotic taxa is relatively high, in

particular in the lower part of the zone. The reconstructed T_{July} is 0.6–2.6 °C below modern air temperature.

In CZ V (15.3–11.4 cal ka BP; 13.9–8.9 mcd) at 14.4 cal ka BP (12.2 mcd) *Hydrobaenus lugubris*-type taxa decline and then disappear from the fauna, while phytophilic taxa (i.e. *Tanytarsus pallidicornis*-type, *Corynoneura arctica*-type and *Cricotopus cylindraceus*-type) appear. The sum of the lotic taxa reaches 40% at the bottom (15.3–14.6 cal ka BP; 13.9–12.5 mcd) and top (11.9 cal ka BP; 9.4 mcd) of the zone and declines to 0 between 13.1 and 12.2 cal ka BP (10.6 and 9.7 mcd). The reconstructed T_{July} show a short decline to 6.9 °C at 15.1 cal ka BP (13.4 mcd) and thereafter remain between 9.1 and 10.5 °C, hence slightly below modern.

In CZ IV (11.4–8.9 cal ka BP; 8.9–6.6 mcd) *H. grimschawi*-type, *Paratanytarsus* and *Micropsectra insignilobus*-type taxa increase. The sum of lotic taxa has a maximum at 10.7 cal ka BP (8.2 mcd). Reconstructed T_{July} are higher than present at 11.1 cal ka BP (8.7 mcd; 12.3 °C) and slightly lower above.

The fauna of CZ III (8.9–5.2 cal ka BP; 6.6–3.4 mcd) is dominated by *H. grimschawi*-type, in the presence of further taxa: *T. pallidicornis*-type and *C. cylindraceus*-type. Towards the top of the zone, the number of lotic taxa and the *Smittia-Parasmittia* and *Limnophyes-Paralimnophyes* increase. The reconstructed T_{July} are the highest recorded, reaching up to 4.8 °C higher than today's air temperature.

H. grimschawi-type and *C. cylindraceus*-type taxa decrease towards the top of CZ II (5.2–1.3 cal ka BP; 3.4–0.7 mcd),
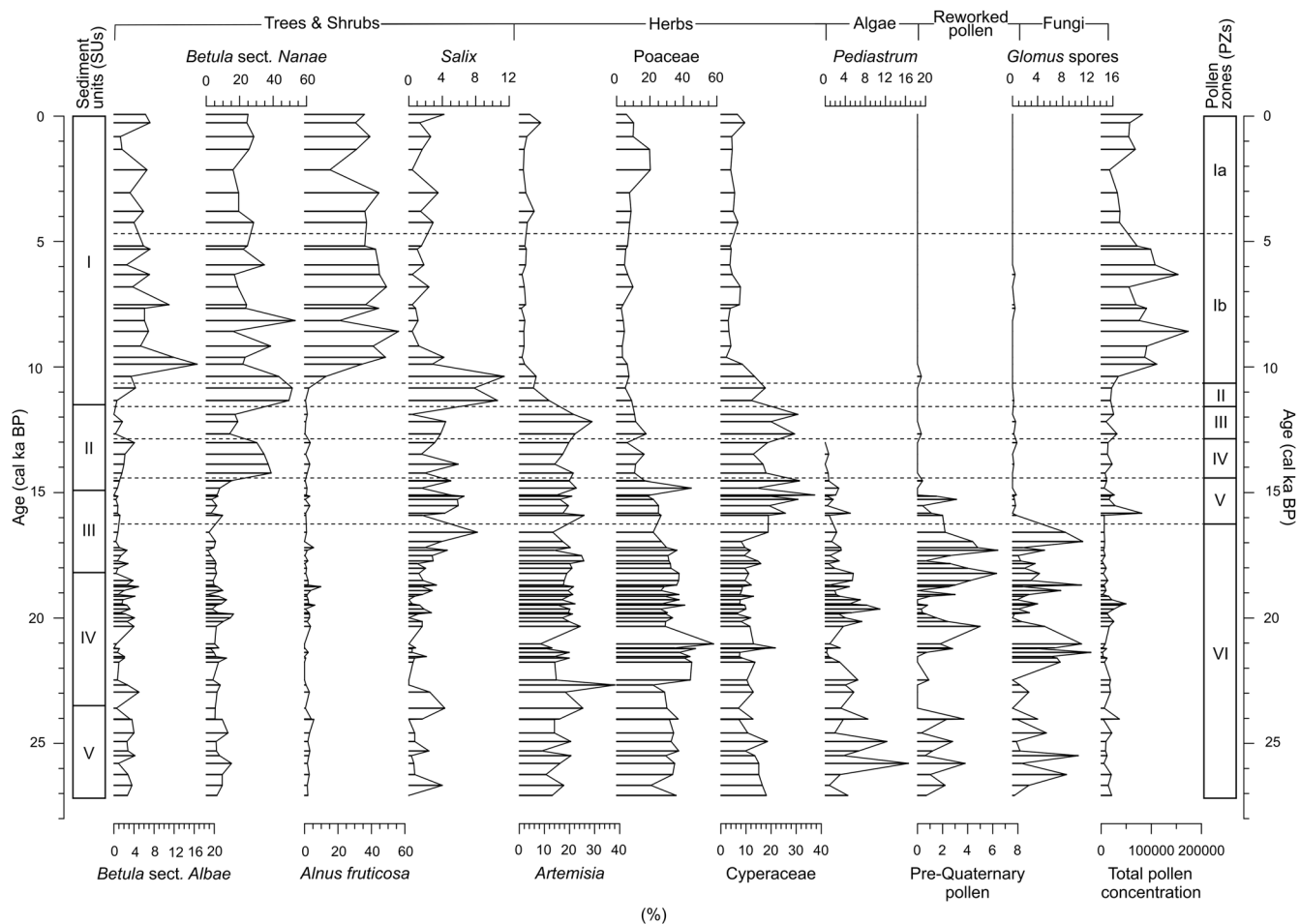
Figure 5. Percentage diagram presenting the main results of the pollen analysis on core Co1321. The pollen assemblages can be subdivided into six main pollen zones (PZ I–VI).

whereas the abundance of *H. subpilosus*-type taxa increase. Lotic taxa are limited and disappear from the chironomid community between 3.9 and 3.3 cal ka BP (2.4 and 2 mcd). The reconstructed T_{July} gradually decrease until 1.8 cal ka BP (1.0 mcd), where they are ~1.3 °C below the present-day T_{July}.

The uppermost section of core CZ I (1.3–0 cal ka BP; 0.7–0 mcd), is characterised by *H. grimschawi*-type and *C. cylindraceus*-type taxa in the fauna. *Chironomus plumosus*-type taxa appear in the record. Simultaneously, the sum of lotic taxa (e.g. *Diamesa* sp., *Tvetenia bavarica*-type, *Thienemanniella clavicornis*-type, *Metriocnemus*) increases. Reconstructed T_{July} indicate slightly warmer T_{July} between 1.2 and 0.7 cal ka BP (0.7 and 0.4 mcd) and decrease to modern temperatures towards the top of CZ I.

LOCAL CLIMATE, GLACIAL AND VEGETATION HISTORY

Glacial influence during the LGM

Our age–depth model proposes that SUs V and IV were deposited between *c.* 27 and 18 cal ka BP (Fig. 7), thus mostly covering the LGM. During this period, the pollen spectra in core Co1321 (low total pollen concentrations and high amounts of herb pollen) reflect an open, herb and grass-dominated tundra-steppe vegetation and inferred cold and/or dry climatic conditions. Increased amounts of *Glomus* spores indicate disturbed soils around the lake (Andreev *et al.*, 2011). TOC/TN around or less than 10 and relatively positive $\delta^{13}C_{org}$

around -26.1‰ argue for low contribution of land plants to the OM deposition (Meyers, 1997; Gundelwein, 1998; Meyers, 2003) and consequently low input of isotopically light soil-derived CO_2 (Hammarlund, 1993; Turney, 1999; Balascio and Bradley, 2012), which again supports the view that the catchment was sparsely vegetated. The rare tree and shrub pollen, i.e. *Pinus* and *Picea* are presumably of long-distance origin, transported to the study area by wind, which is a known phenomenon in the Arctic (e.g. Gajewski *et al.*, 1995). Growth of distal trees may have been favoured in ice-free regions by moderately warm temperatures during the growing season (Clarke *et al.* 2020). Accordingly, the chironomid-inferred T_{July} points to local summer air temperatures only 1.2–2.6 °C below present air temperatures. Summer temperatures during the LGM may not have been much colder than today, as summer insolation (Fig. 7; Laskar *et al.*, 2004; Berger *et al.*, 2010) was also at a similar level. This climatic reconstruction for the area of Lake Bolshoye Shchuchye agrees very well with palaeoecological studies (e.g. pollen, plant macrofossils, insects) and model simulations reporting a cold and dry LGM climate across northern Eurasia (Hubberten *et al.*, 2004; Andreev *et al.*, 2011), with winters 7–15 °C colder, summers 1–7 °C colder and precipitation sums 50–750 mm lower than today (Tarasov *et al.*, 1999).

The upward increase and lack of distinct shifts in water content or other abrupt and marked sedimentological transitions suggest the absence of hiatuses or disturbances of sedimentation, such as those caused by grounding glacier ice. This result supports the suggestion of Regnéll *et al.* (2019) and Svendsen *et al.* (2019) that the lake basin was not
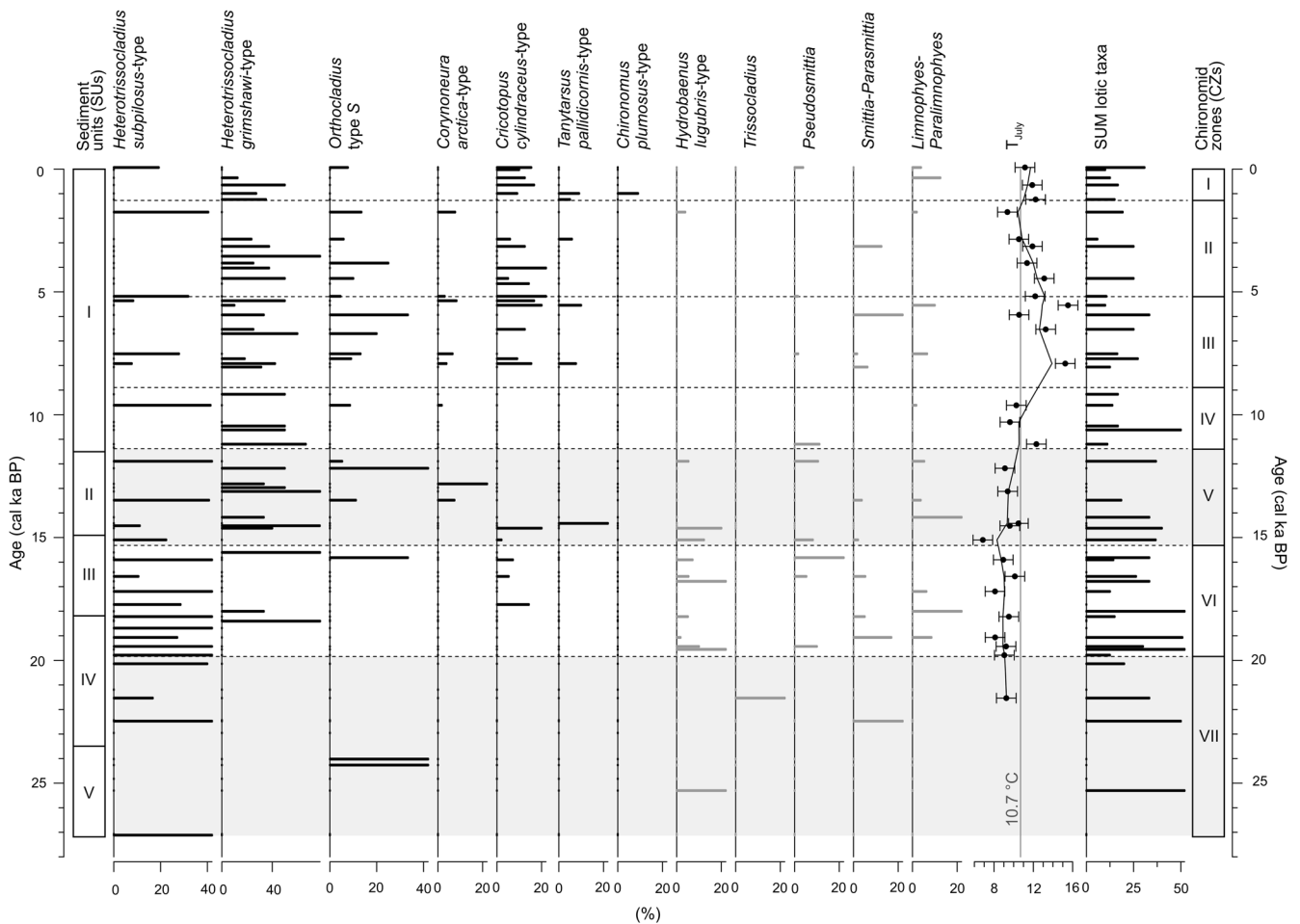
Figure 6. Relative proportions of the most abundant chironomid taxa in core Co1321, along with the chironomid-inferred mean air temperatures in July (T_{July} in °C), the sum of lotic taxa, and differentiation into seven chironomid zones (CZ I–VII). The grey shading marks zones, in which the analysed sediment samples contained relatively low amounts of chironomid remains. Grey bars indicate lotic taxa. The T_{July} are displayed as data points with respective error bars. The black line running through these data points represents the LOESS 0.2 smooth of the data and the grey line indicates the modern T_{July} of 10.7 °C.

overridden by glacier ice during the LGM. The catchment area of the lake, on the other hand, was apparently occupied by local glaciers, which supplied fine-grained clastic material and produced strong lamination, as revealed by the high clay content and deposition of glacial varves (Figs. 3, 4 and 7; Blott and Pye, 2001; van der Bilt *et al.*, 2016). Partly high total amounts of lotic taxa (e.g. *Metriocnemus*, *Thienemanniella clavicornis*-type, *Diamesinae* sp.), characteristic of flowing water (Moller Pillot, 2009), indicate that during glacial ablation in spring to summer, meltwater runoff was occasionally high. High abundancies of *H. lugubris*-type chironomids, which thrive in the inundated areas of river floodplains (Steinhart, 2000), further suggest that the abundant supply of meltwater at times led to flood events and the formation of shallow littorals in some flat areas and depressions within the lake catchment. Remains of green algae colonies (*Pediastrum*) and semi-terrestrial *Trissocladius* taxa support the suggestion that shallow freshwater habitats or temporary to permanent pools existed around the lake (Jankovská and Komárek, 2001; Brooks *et al.*, 2007; Andreev *et al.*, 2011).

Our interpretation is in accordance with dating results on glaciofluvial deposits (water-transported boulders, a relict glaciofluvial fan system) in the main valley north of the lake (Fig. 1B), where most of the sediment input came from at that time (Haflidason *et al.*, 2019). The deposits are assumed to have been transported by meltwater streams draining glaciers within the higher mountain valleys and cirques during the LGM (Svendsen *et al.*, 2019). Part of the sediment input from

the north presumably comprised sediments that were deposited during the preceding MIS 4 glaciation and resedimented during the LGM as a result of efficient glacial and stream erosion. Therefore, we suspect that the frequent pre-Quaternary palynomorphs are reworked from tills or other sediments brought into the catchment by the MIS 4 ice sheet (Gajewski *et al.*, 1995; Svendsen *et al.*, 2014). High numbers of semi-terrestrial chironomid taxa (*Smittia-Parasmittia*; Fig. 6) confirm our suggestion that catchment erosion, which was supposedly also favoured by the disturbed soils (Hubberten *et al.*, 2004), was high (Nazarova *et al.*, 2015b, 2018).

Some sediment input may also have come from the southern part of the catchment as evidenced by partly elevated TIC content, which most likely originated from detrital carbonate in the bedrock. For TIC a biogenic source can be excluded because the sediment is devoid of carbonate fossils. Also, endogenic calcite precipitation in a cold Arctic lake like Bolshoye Shchuchye can be regarded as negligible (Last and Smol, 2001; Cohen, 2003). Given the limitation of carbonate exposures to the hillsides surrounding Lake Bolshoye Shchuchye in the west and east (Fig. 2), the TIC content may be a sensitive proxy for sediment supply from these regions. Exposure dates on a moraine ridge in the Hynotayakha Valley south-west of Lake Bolshoye Shchuchye (Hynotayakha moraine) yielded a mean value of 23.8 ± 3.7 (Fig. 1B), which supports the view that at least the western hillside of the lake was occupied by a local glacier (Svendsen *et al.*, 2019). At its maximum extent, it is assumed that the glacier which
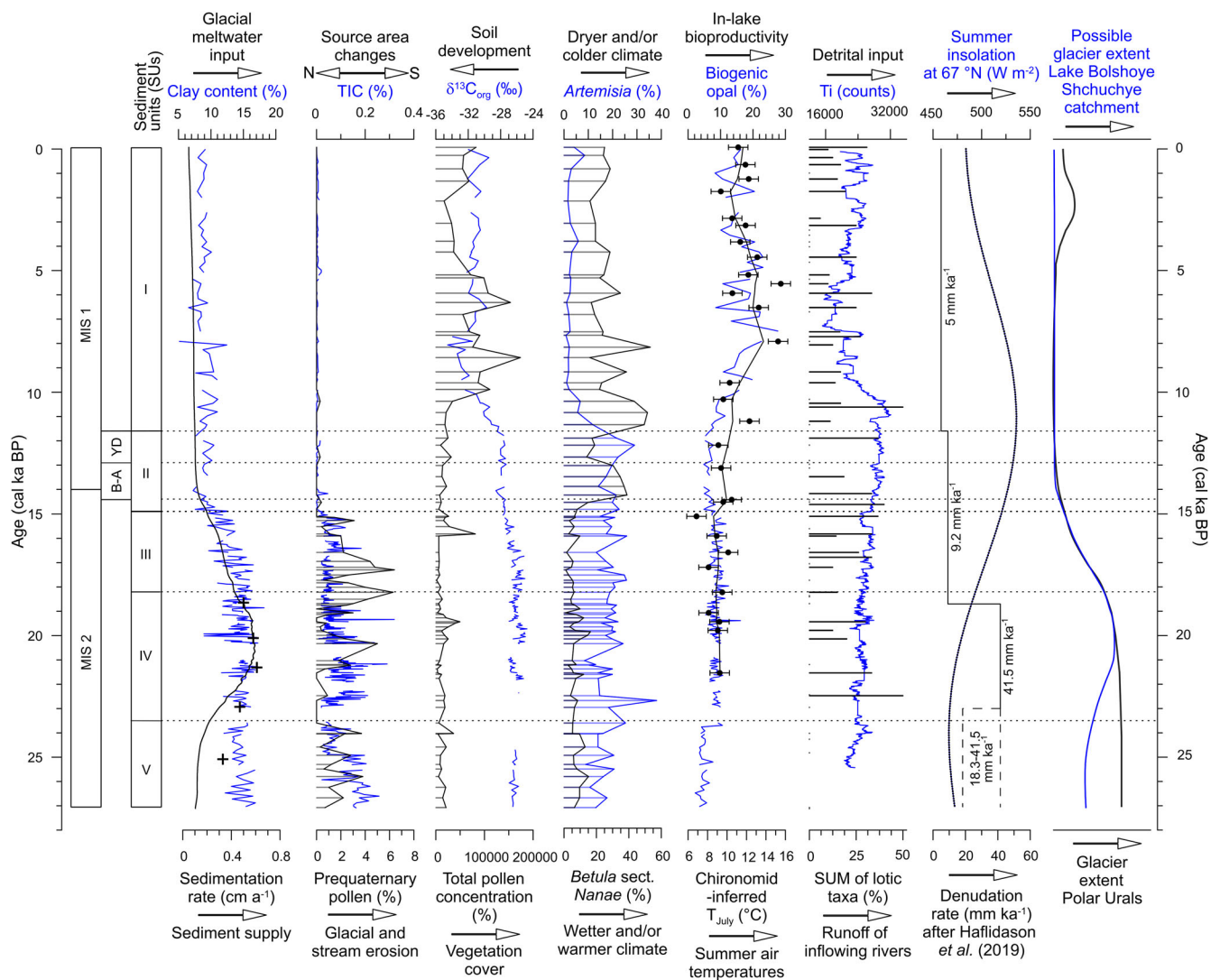
Figure 7. Selected physical and geochemical proxy data (MS = magnetic susceptibility, TIC = total inorganic carbon, TOC = total organic carbon), pollen percentages and chironomid-inferred summer air temperatures from core Co1321 plotted against age. The black line running through the T_{July} data points represents the LOESS 0.2 smooth of the data. The plot describing the sedimentation rate shows the mean sedimentation rate (solid line; red line in Fig. 3) and the results of the varve count (crosses). The data are shown together with the Marine Isotope Stages following Lisiecki and Raymo (2005), the estimated denudation rate for each of the seismo-stratigraphical units (Haflidason *et al.*, 2019), summer insolation at 67°N (Laskar *et al.*, 2004; Berger *et al.*, 2010) and a reconstruction δ of glacier ice extent in the Lake Bolshoye Shchuchye catchment (based on our data) and the polar Urals (Svendsen *et al.*, 2019). [Color figure can be viewed at wileyonlinelibrary.com].

deposited the Hynotayakha moraine flowed out of the Sehrmalyakha Valley towards the southern end of Lake Bolshoye Shchuchye (Svendsen *et al.*, 2019). Such a scenario may also explain the coarse-grained sediments underlying core PG506-48/50 from the southern part of the lake, which were dated to 25–24 cal ka BP (Haflidason *et al.*, 2019), but the absence of such sediments at that time at site Co1321 from the central part of the lake.

The relatively high supply of fine-grained clastic material between *c.* 27 and 18 cal ka BP led to a high suspension load and thereby limited light-penetration and primary productivity in the lake, as suggested by overall low TOC and BO content and the lack of bioturbation in the sediments (Meyers and Ishiwatari, 1993; Cohen, 2003; Davies *et al.*, 2015). The slightly increased BO values in SU IV between *c.* 23.5 and 18 cal ka BP probably do not reflect increased aquatic production but rather better preservation, perhaps in dependence of the higher sedimentation rate (Swann and Mackay, 2006). The chironomid fauna is composed of cold-stenothermic, oligotrophic and acid-tolerant taxa (*H. subpilosus*-type, *Hydrobaenus lugubris*-type, *Orthocladius* type *S*).

Anoxic bottom water conditions are therefore unlikely, because bacterial oxygen consumption during OM decomposition is low or negligible in such oligotrophic lakes (e.g. Wagner and Cremer, 2006). This assumption is supported by relatively low instead of elevated TOC content, as is commonly the case in anoxic bottom waters due to the enhanced preservation of OM (Melles *et al.*, 2007). Moreover, this interval shows elevated rather than reduced MS values. Considering the missing indication for the occurrence of greigite (see supplementary material for details), it can be assumed that no dissolution of the magnetic mineral fraction (especially ferromagnetic minerals like magnetite) took place under anoxic conditions (Nowaczyk *et al.*, 2007).

The relatively low and steady sand input (averaged over several varves) may originate from turbidites, which were not omitted during sampling in the case of a layer thickness of <1 cm. Alternatively, the continental setting of Lake Bolshoye Shchuchye (Regnéll *et al.*, 2019) may have favoured ice break-up in summer, allowing the sand to be carried into the lake by fluvial input or lake-ice rafting. Considering that Lake Bolshoye Shchuchye is ice-free for a maximum of three summer months

under the present climate, it is also possible, however, that the colder climate during the LGM favoured year-round (or almost year-round) ice cover of the lake (Regnéll et al., 2019).

Core Co1321 records the highest sediment input during the deposition of SU IV between c. 23.5 and 18 cal ka BP, by maxima in glacial varve thickness and sedimentation rates (Figs. 3 and 7). The exceptionally high sediment flux was also recorded in core PG50-48/50 (2.2–2.6 mm a^{-1}) during the period 23.8 and 18.7 cal ka BP. The distinct increase in sediment supply around 24 ka may be related to higher melt rates in spring to summer during an early phase of glacial retreat (Leonard, 1986; Eyles and Clague, 1991; Ballantyne, 2002). This conclusion would be in line with Svendsen et al. (2019), who propose that glacial extension culminated before c. 24 cal ka BP, either during an early phase of MIS 2 or a late phase of MIS 3. However, this was a period with relatively low summer insolation (Fig. 7; Laskar et al., 2004; Berger et al., 2010) and low summer air temperatures, as indicated by the chironomid data (Figs. 6 and 7). Alternatively, the exceptionally high sedimentation rate may be attributed to a more expanded and thus more proximal position of the ice margin and/or glacial rerouting towards the lake (Leemann and Niessen, 1994; Davies et al., 2015; Arnaud et al., 2016). This conclusion would imply that local glaciers attained their maximum size shortly after c. 23.5 cal ka BP.

Concurrent with the increased sedimentation rate, maxima in turbidite frequency and cumulative thickness occur (Fig. 3). This correlation reflects the suggestion that the increase in sedimentation rate was due to increases in both hemipelagic (varve) and gravitational (turbidite) deposition. Both processes were likely triggered by increased glaciofluvial sediment supply. The sediment clearly included a lot of old, redeposited OM (maximum amounts in pre-Quaternary palynomorphs; Figs. 5 and 7) and inorganic carbon (high TIC; Figs. 4 and 7) as suggested by the simultaneous maximum in the reservoir effect (Fig. 3; Björck and Wohlfarth, 2002).

The deglaciation of the lake catchment

The deglaciation of the catchment of Lake Bolshoye Shchuchye is recorded between c. 18 and 15 cal ka BP by a gradual decrease in glacial varve formation and sediment supply to the lake. This development is indicated by a progressive change from distinctly laminated to diffusely layered sedimentation and steady decreases in sedimentation rates and clay content. The changes (in lithology and sedimentation rates) occur simultaneously with those described in core PG506-48/50 (18.7–14.35 cal ka BP; Regnéll et al., 2019). As a consequence of the lower sediment flux, gravitational (turbidite) deposition became less. The pronounced decrease in sediment discharge during this period is confirmed by a significantly decreased denudation rate in the Lateglacial (Fig. 7; Haflidason et al., 2019).

In accordance with glacier retreat, abundancies of lotic taxa show a decrease as riverine discharge became less. Significantly lower amounts of green algal spores (Pediastrum), yet high numbers of H. lugubris-type chironomids, contradict our interpretation that both species indicate shallow-water areas in the lake watershed during the LGM. We can only speculate that the lower runoff of meltwater resulted in fewer floodplains and that the H. lugubris-type chironomids because of their high adaptability survived in pools and puddles even after the floodplains dried out (Steinhart, 2000). Such a scenario would concur with the interpretation of Svendsen et al. (2019), who suggested that, based on the aforementioned ^{10}Be dates on water-transported boulders on top of relict terraces in the Pyryantanë Valley, meltwater discharge was high until c. 19 ka

and fluvial incision started thereafter. The pronounced deglaciation of the lake catchment was likely triggered by an increase in summer insolation after c. 20 ka (Fig. 7; Laskar et al., 2004; Berger et al., 2010), which also initiated the recession of the Eurasian Ice Sheet complex (Miller et al., 2010; Hughes et al., 2016; Clarke et al., 2020). Accordingly, the reconstructed T$_{July}$ were 0.6–0.8 °C warmer than during the LGM.

Around 17–16 cal ka BP, the pollen spectra indicate a distinct shift to moderate pollen concentrations and increases in the content of Cyperaceae and Salix. This PZ VI/V boundary corresponds well with the results of Clarke et al. (2020) on core PG506-48, who report an increase in Cyperaceae in the pollen record from c. 16 cal ka BP and in the sedimentary ancient DNA (sedaDNA) already from c. 17 cal ka BP. Together with increases in floristic richness, sedges and bryophytes, they interpret these changes as a shift to moister conditions. A simultaneous decline in the number of Glomus spores and slightly decreasing δ^{13}C$_{org}$ ratios, which can originate from soil-derived CO$_2$ from root respiration and humic acid decomposition (Hammarlund, 1993; Turney, 1999; Balascio and Bradley, 2012), support the idea that the vegetation cover became somewhat denser (Andreev et al., 2011). At the same time, relatively low TOC content and TOC/TN < 7 point to a low productivity environment, probably in combination with some decomposition of OM. The observed environmental changes are synchronous with warmer and moister conditions recorded on the Taymyr Peninsula and in the Laptev Sea region from 16–12 ka (Andreev et al., 2011). Clarke et al. (2020) argue that a marked increase in the recession rate of the Eurasian Ice Sheet complex around 16 cal ka BP (Clark et al., 2009; Miller et al., 2010; Hughes et al., 2016) likely led to this increase in moisture availability within the polar Urals and beyond.

The declines in redeposited pre-Quaternary microfossils and TIC content at c. 15 cal ka BP evidence that clastic input from the hillsides to the west and east of Lake Bolshoye Shchuchye became negligible, when the glaciers occupying these mountains had disappeared. This change in sediment provenance suggests that after c.15 cal ka BP the catchment has become similar to today, with pronounced sediment input coming from the Pyryantanyë River at the northern end of the lake. Nevertheless, high MS, Ti and silt content suggests that the minerogenic sediment supply from the catchment remained high during this interval. Possible causes include a still relatively unstable, scarcely vegetated catchment and/or enhanced riverine runoff from rainfall.

The Bølling-Allerød and Younger Dryas

The Bølling-Allerød, starting at 14 565 cal a BP (Bjune et al., this issue), is reflected in the pollen data of core Co1321 by distinctly increased amounts of dwarf birch (Betula sect. Nanae), whereas the total pollen concentration remains moderate and herb pollen (Artemisia and Cyperaceae) is still in relatively high amounts. An expansion of dwarf birch during the Bølling-Allerød has also been reported in the pollen record from the nearby Lake Gerdizty (Svendsen et al., 2014) and Lake Yamozero (Henriksen et al., 2008), as well as from the Timan Ridge (Paus et al., 2003) and Yamal Peninsula (Andreev et al., 2006). At that time, the chironomid fauna records a clear shift from cold-stenotherm taxa to taxa characteristic for warmer conditions and summer air temperatures similar to modern (0.2–1.3 °C cooler than today). Climatic warming apparently led to the complete disappearance of local glaciers at the beginning of the Bølling-Allerød, as indicated by relatively low sedimentation rates and clay content since then.

Relatively high amounts of lotic taxa during the Bølling-Allerød may therefore imply occasionally high riverine runoff from rainfall events, which is in accordance with the results of Cowling *et al.* (this issue). The authors reconstructed an increase in summer precipitation at our study from site *c.* 14.5 cal ka BP based on enriched hydrogen isotope values derived from long-chain leaf waxes. Increases in TOC and TOC/N and more negative $\delta^{13}C_{org}$ values demonstrate that the warmer and more humid conditions led to increased terrestrial productivity and soil development in the lake's catchment.

During the Younger Dryas, the pollen spectra show lower content of dwarf birch (*Betula* sect. *Nanae*) together with slightly higher amounts of herb pollen (*Artemisia* and Cyperaceae), such as reported in other regional pollen records (e.g. Paus *et al.*, 2003; Andreev *et al.*, 2006, 2011; Henriksen *et al.*, 2008). The chironomid population in core Co1321 shows an increase in cold-stenotherm taxa, thereby confirming cooler climate conditions. Marked disappearances of lotic taxa (Figs. 6 and 7) and *Pediastrum* remains (Fig. 5) furthermore suggest that fluvial supply was extremely low, likely associated with very dry conditions. On the basis of their data, Cowling *et al.* (this issue) propose that the climate may have been as dry as during the LGM. However, as evidenced by constantly low sedimentation rates and low clay input, glaciers did apparently not regrow in the vicinity of Lake Bolshoye Shchuchye, thereby supporting the respective interpretation of Haflidason *et al.* (2019). The better-dated record PG506-48 of pollen and sedaDNA (Bjune *et al.*, this issue) furthermore reveals that the onset of the Younger Dryas cooling at Lake Bolshoye Shchuchye started about 300 years earlier than at other key sites, for instance in Greenland or Norway (Rasmussen *et al.*, 2006; Lohne *et al.*, 2014; Seierstad *et al.*, 2014). This finding could indicate that the vegetation at Lake Bolshoye Shchuchye reacted during the Allerød at 13.1 cal ka BP and did not recover during the late Allerød.

Climate and environmental changes during the Holocene

The age–depth model suggests an accumulation of SU I between *c.* 11.5 cal ka BP and today, hence during the Holocene. The onset of the Holocene is marked by notable increases in dwarf birch and willow (*Betula* sect. *Nanae and Salix*), TOC and BO content and TOC/TN ratios together with decreases in herb pollen (especially *Artemisia*) and $\delta^{13}C_{org}$ values. The proxies indicate an increase of terrestrial as well as aquatic productivity with substantial nutrient input from the catchment. Rapid decreases in MS and Ti indicate that a progressively denser vegetation cover and soil development stabilised the catchment and reduced the minerogenic material input, as confirmed by a reduction in the denudation rate (Haflidason *et al.*, 2019). The chironomid fauna shows an increase in taxa characteristic for milder conditions (*H. grimschawi*-type, *Paratanytarsus* and *Micropsectra insignilobus*-type), whereas cold-stenotherm *H. subpilosus*-type taxa decrease. According to the chironomid-based temperature reconstruction, summer air temperatures at this time rose up to 1.6 °C above modern. A full description and discussion on tree immigration in the Holocene is provided by Clarke *et al.* (2020).

The highest productivity in and around the lake can be inferred between *c.* 10 and 5 cal ka BP by the highest recorded total pollen concentrations, dominance of shrub and tree pollen taxa (especially *Betula* sect. *Albae*, *Alnus fruticosa*), high TOC and BO content, particularly light $\delta^{13}C_{org}$ ratios and lowest percentages of herbs (*Artemisia*, Poaceae, Cyperaceae). The productivity peak coincides with a dominance of warm-stenotherm *H. grimschawi*-type taxa in the chironomid fauna and chironomid-inferred T_{July} of up to 4.8 °C warmer than

present. A simultaneous minimum in Ti and MS demonstrates that the detrital input was greatly restricted. Nevertheless, after *c.* 10 cal ka BP, relatively high variability of MS, TOC and BO values and partly high numbers of lotic taxa and taxa characteristic for erosion and redeposition (especially *Smittia-Parasmittia* and *Limnophyes-Paralimnophyes*) point to relatively unstable environmental conditions. During this period, Cowling *et al.* (this issue) report an abrupt ^{2}H-enrichment (from 10.5 cal ka BP) related to increased summer precipitation and possibly other changes such as those related to lake-water mixing and evaporation. They attribute the higher precipitation to changes in moisture transport from the North Atlantic due to the final disappearance of the Scandinavian Ice Sheet at 10 ka (Hughes *et al.*, 2016), a substantial decrease in sea ice cover in the Barents-Kara Seas (Brendryen *et al.*, 2020), or most probably a substantial increase in locally evaporated moisture due to the northward treeline expansion into the polar Urals and surrounding lowlands (Clarke *et al.*, 2020).

The local Holocene Thermal Maximum (HTM) may have been caused by orbitally forced regional warmth following the maximum in summer insolation ~11 ka ago (Fig. 7; Laskar *et al.*, 2004; Berger *et al.*, 2010; Miller *et al.*, 2010; Solomina *et al.*, 2015). An early to mid-HTM has also been reported in pollen records from Lake Lyadhey-To in the north-western polar Ural Mountains (Andreev *et al.*, 2005), Timan Ridge (Paus *et al.*, 2003), the Yamal Peninsula (Forman *et al.*, 2002) and Lake Levinson-Lessing on the Taymyr Peninsula (Andreev *et al.*, 2003).

After *c.* 5 cal ka BP the climate became colder and the present-day treeless dwarf-shrub tundra environment began to develop near the lake. This change is reflected by an increase in herb pollen and a decline in total pollen concentration, *Alnus fruticosa* and *Betula* sect. *Albae* pollen percentages and is in good agreement with previous studies from mainland Eurasia (Paus *et al.*, 2003; Andreev and Tarasov, 2013; Regnéll *et al.*, 2019). The diversity of lotic chironomids decreases to a minimum around 4 cal ka BP, which indicates reduced inflow from the surrounding rivers. Chironomid-inferred T_{July} imply 1.3 °C cooler than modern air temperatures at 1.8 cal ka BP, and slightly warmer T_{July} between 1.2 and 0.7 cal ka BP, possibly associated with the Little Ice Age (about 1850–1250 AD; Solomina *et al.*, 2016) and the Medieval Warm Period (1250–950 AD; Solomina *et al.*, 2016), respectively. Cooler temperatures during the Little Ice Age may have allowed the recent small glaciers in the polar Urals that exist in some shady cirques to regrow (Svendsen *et al.*, 2019). However, our geochemical proxies show no changes at that time, suggesting that the catchment of Lake Bolshoye Shchuchye remained ice free. Present-day T_{July} have persisted since 0.5 cal ka BP.

CONCLUSIONS

The 54 m long sediment core retrieved from the central lake basin of Bolshoye Shchuchye represents a unique high-resolution archive. A synthesis of multiproxy data allowed us to reconstruct climate, glacial and environmental changes affecting the polar Urals during the last *c.* 27 cal ka BP.

- Sedimentological data indicate that the lake received melt-water and sediments from the local glaciers from *c.* 27 until the onset of the Bølling-Allerød warming, when the glaciers disappeared completely from the catchment area.
- Pollen analysis reveals an open vegetation dominated by herbs and grasses prior to the Holocene, except for the Bølling-Allerød interstadial when shrubs increased distinctly. Trees were growing around the lake in the early to

mid-Holocene when the climate was warmer than today and a low shrub tundra established after *c.* 5 cal ka BP. The opposite trends in total pollen concentrations as proxy for vegetation growth and $\delta^{13}C_{org}$ ratios in core Co1321 suggest that $\delta^{13}C_{org}$ can be used as sensitive proxy of soil development.

- The chironomid record indicates relatively cold and dry climate conditions and about 1–2 °C colder than modern summer air temperatures during the LGM and Younger Dryas. During the Bølling-Allerød and Holocene, climate conditions were relatively warm and wet with a local HTM (about 2 °C warmer than today) from *c.* 10–5 cal ka BP. The data may further depict air temperature changes during the Little Ice Age and Medieval Warm Period. Simultaneous changes in T_{July} and BO suggests that summer air temperatures predominantly controlled in-lake productivity at Lake Bolshoye Shchuchye.

Supporting information

Additional supporting information can be found in the online version of this article.This article includes online-only Supplemental Data.

Table S1. Hysteresis parameters of selected samples for mineral magnetic analysis. The Bcr value of the sample of 572.6 cm is missing due to a device failure.

Figure S1. The temperature dependency of the magnetic susceptibility. Only heating curves are shown. (a) comparison of all measurements. (b) Results of samples from 53.64, 50.36, 42.51, 32.52, 20.05 and 14.27 mcd. (c) Results of samples from 12.20 and 8.99 mcd. (d) Results of samples from 5.73 and 0.64 mcd.

Figure S2. The Néel diagram (Néel, 1955), changed after Tauxe *et al.* (2002). Except for the samples from 42.51 and

14.27 the samples reveal dominance of stable single domain (SD) or pseudo-single domain (PSD) behaviour.

Figure S3. Quality of the mean July air temperature (T_{July}) reconstruction, using the chironomid-based temperature inference model (Nazarova *et al.*, 2015a). MAT for modern analogue technique; vertical grey lines show percentiles of the modern data set: cut-levels of the 5th (26.873) and 10th (30.4025) percentiles of all squared $\chi 2$-distances in the modern calibration data set define 'no close' and 'no good' analogues when comparing the distance between an individual fossil assemblage and the most similar assemblage in the modern data set. In red are shown the reconstructions with 'no good' analogues.

References

Andreev AA, Tarasov PE, Siegert C *et al.* 2003. Late Pleistocene and Holocene vegetation and climate on the northern Taymyr Peninsula, Arctic Russia. *Boreas* **32**: 484–505.

Andreev AA, Tarasov PE, Ilyashuk BP *et al.* 2005. Holocene environmental history recorded in Lake Lyadhej-To sediments, Polar Urals, Russia. *Palaeogeography Palaeoclimatology Palaeoecology* **223**: 181–203.

Andreev AA, Forman SL, Ingólfsson O *et al.* 2006. Middle Weichselian environments on western Yamal Peninsula, Kara Sea based on pollen records. *Quaternary Research* **65**: 275–281.

Andreev AA, Schirrmeister L, Tarasov PE *et al.* 2011. Vegetation and climate history in the Laptev Sea region (Arctic Siberia) during Late Quaternary inferred from pollen records. *Quaternary Science Reviews* **30**: 2182–2199.

Andreev AA, Morozova E, Fedorov G *et al.* 2012. Vegetation history of central Chukotka deduced from permafrost paleoenvironmental records of the El'gygytgyn Impact Crater. *Climate of the Past* **8**: 1287–1300.

Andreev AA, Tarasov PE. 2013. Pollen records, postglacial: Northern Asia. In *Encyclopedia of Quaternary Science*, Elias SA, Mock CJ (eds). Elsevier: Amsterdam.164–172.

Arnaud F, Poulenard J, Giguet-Covex C *et al.* 2016. Erosion under climate and human pressures: An alpine lake sediment perspective. *Quaternary Science Reviews* **152**: 1–18.

Astakhov V. 2018. Late Quaternary glaciation of the northern Urals: a review and new observations. *Boreas* **47**: 379–389.

Astakhov V, Nazarov D. 2010. Correlation of Upper Pleistocene sediments in northern West Siberia. *Quaternary Science Reviews* **29**: 3615–3629.

Balascio NL, Bradley RS. 2012. Evaluating Holocene climate change in northern Norway using sediment records from two contrasting lake systems. *Journal of Paleolimnology* **48**: 259–273.

Ballantyne CK. 2002. A general model of paraglacial landscape response. *The Holocene* **12**: 371–376.

Berger A, Loutre M-F, Yin Q. 2010. Total irradiation during any time interval of the year using elliptic integrals. *Quaternary Science Reviews* **29**: 1968–1982.

Berglund BE, Ralska-Jasiewiczowa M. 1986. Pollen analysis and pollen diagrams. In *Handbook of Holocene Palaeoecology and Palaeohydrology*, Berglund BE (ed). John Wiley and Sons Press: Chester.455–484.

Birks H, Braak CT, Line J *et al.* 1990. Diatoms and pH reconstruction. *Philosophical transactions of the royal society of London. B, Biological Sciences* **327**: 263–278.

Björck S, Wohlfarth B. 2002. 14C chronostratigraphic techniques in paleolimnology. In *Tracking environmental change using lake sediments. Basin Analysis, Coring, and Chronological Techniques*, Last WM, Smol JP (eds). Springer: Dordrecht.205–245.

Bjune AE, Alsos I, Brendryen J *et al.* *Journal of Quaternary Science* this issue Rapid climate changes during the Late Glacial and the early Holocene as seen from plant community dynamics in the Polar Urals, Russia.

Blaauw M. 2010. Methods and code for 'classical' age-modelling of radiocarbon sequences. *Quaternary Geochronology* **5**: 512–518.

Blaauw M. 2021. Clam: Classical Age-Depth Modelling of Cores from Deposits. R package version 2.3.9.

Blaauw M, Christen JA. 2011. Flexible paleoclimate age-depth models using an autoregressive gamma process. *Bayesian Analysis* **6**: 457–474.

Blott SJ, Pye K. 2001. GRADISTAT: a grain size distribution and statistics package for the analysis of unconsolidated sediments. *Earth Surface Processes and Landforms* **26**: 1237–1248.

Bobrov AE, Kupriyanova LA, Litvintseva MV et al. 1983. *Spores and Pollen of Gymnosperms from the Flora of the European Part of the USSR*, Leningrad (in Russian), Nauka.

Brendryen J, Haflidason H, Yokoyama Y et al. 2020. Collapse of Eurasian ice sheets 14,600 years ago was a major source of global Meltwater Pulse 1a. https://doi.org/10.31223/osf.io/7g5bn

Brook S, Langdon P, Heiri O. 2007. *The identification and use of Palearctic Chironomidae larvae in palaeoecology. QRA Technical Guide No. 10*, London, Quaternary Research Association.

Brooks SJ, Birks HJB. 2001. Chironomid-inferred air temperatures from Lateglacial and Holocene sites in north-west Europe: progress and problems. *Quaternary Science Reviews* **20**: 1723–1741.

Channell JET, Hodell DA, Crowhurst SJ et al. 2018. Relative paleointensity (RPI) in the latest Pleistocene (10–45 ka) and implications for deglacial atmospheric radiocarbon. *Quaternary Science Reviews* **191**: 57–72.

Clark PU, Dyke AS, Shakun JD et al. 2009. The Last Glacial Maximum. *Science* **325**: 710–714.

Clarke CL, Alsos IG, Edwards ME et al. 2020. A 24,000-year ancient DNA and pollen record from the Polar Urals reveals temporal dynamics of arctic and boreal plant communities. *Quaternary Science Reviews* **247**: 106564.

Cohen AS. 2003. *Paleolimnology: The History and Evolution of Lake Systems.* Oxford University Press: New York.

Cowling O, Thomas E, Svendsen JI et al. Journal of Quaternary Science this issue. The hydrologic cycle in western Siberia during the past 24,000 years changed in step with plant community structure.

Davies SJ, Lamb HF, Roberts SJ. 2015. Micro-XRF Core Scanning in Palaeolimnology: Recent Developments. In *Micro-XRF Studies of Sediment Cores*, Croudace IW, Rothwell RG (eds). Springer: Dordrecht.189–226.

Dewald A, Heinze S, Jolie J et al. 2013. CologneAMS, a dedicated center for accelerator mass spectrometry in Germany. *Nuclear Instruments and Methods in Physics Research Section B: Beam Interactions with Materials and Atoms* **294**: 18–23.

Durcan JA, King GE, Duller GAT. 2015. DRAC: Dose Rate and Age Calculator for trapped charge dating. *Quaternary Geochronology* **28**: 54–61.

Dushin VA, Serdyukova OP & Malyugin AA et al. 2009. State Geological Map of the Russian Federation 1:200 000. Sheet Q-42-I, II, St. Petersburg (in Russian), VSEGEI.

Eyles N, Clague JJ. 1991. Glaciolacustrine Sedimentation during Advance and Retreat of the Cordilleran Ice-Sheet in Central British-Columbia. *Géographie Physique et Quaternaire* **45**: 317–331.

Forman SL, Ingólfsson Ó, Gataullin V et al. 2002. Late Quaternary Stratigraphy, Glacial Limits, and Paleoenvironments of the Marresale Area, Western Yamal Peninsula, Russia. *Quaternary Research* **57**: 355–370.

Gajewski K, Garneau M, Bourgeois JC. 1995. Paleoenvironments of the Canadian high arctic derived from pollen and plant macrofossils: Problems and potentials. *Quaternary Science Reviews* **14**: 609–629.

Galbraith RF, Roberts RG, Laslett GM et al. 1999. Optical dating of single and multiple grains of quartz from Jinmium rock shelter, northern Australia. Part I: experimental design and statistical models. *Archaeometry* **41**: 339–364.

Grimm E. 2004. TGView Version 2.0.2. Springfield: Illinois State Museum, Research and Collections Center.

Gundelwein A. 1998. *Eigenschaften und Umsetzung organischer Substanz in nordsibirischen Permafrostböden*, Hamburg (in German), Verein zur Förderung d. Bodenkunde.

Haflidason H, Brendryen J, Elegard RF et al. Journal of Quaternary Science this issue. High resolution chronology of 24 000 years long cores from two lakes in the Polar Urlas, Russia, correlated with paleomagnetic-inclination records with a distinct event about 20 000 years ago.

Haflidason H, Zweidorff JL, Baumer M et al. 2019. The Lastglacial and Holocene seismostratigraphy and sediment distribution of Lake Bolshoye Shchuchye, Polar Ural Mountains, Arctic Russia. *Boreas* **48**: 452–469.

Hammarlund D. 1993. A distinct $\delta^{13}C$ decline in organic lake sediments at the Pleistocene-Holocene transition in southern Sweden. *Boreas* **22**: 236–243.

Hanesch M, Stanjek H, Petersen N. 2006. Thermomagnetic measurements of soil iron minerals: the role of organic carbon. *Geophysical Journal International* **165**: 53–61.

Heiri O, Lotter AF. 2001. Effect of low count sums on quantitative environmental reconstructions: an example using subfossil chironomids. *Journal of Paleolimnology* **26**: 343–350.

Henriksen M, Mangerud JAN, Matiouchkov A et al. 2008. Intriguing climatic shifts in a 90 kyr old lake record from northern Russia. *Boreas* **37**: 20–37.

Hubberten HW, Andreev A, Astakhov VI et al. 2004. The periglacial climate and environment in northern Eurasia during the Last Glaciation. *Quaternary Science Reviews* **23**: 1333–1357.

Hughes ALC, Gyllencreutz R, Lohne ØS et al. 2016. The last Eurasian ice sheets – a chronological database and time-slice reconstruction, DATED-1. *Boreas* **45**: 1–45.

Huntley DJ, Lamothe M. 2001. Ubiquity of anomalous fading in K-feldspars and the measurement and correction for it in optical dating. *Canadian Journal of Earth Sciences* **38**: 1093–1106.

Jankovská V, Komárek J. 2001. *Review of the Green Algal Genus Pediastrum; Implication for Pollen-analytical Research* Berlin: J. Cramer.

Juggins S. 2007. C2: Software for ecological and palaeoecological data analysis and visualisation (user guide version 1.5). *Newcastle upon Tyne: Newcastle University* **77**: 680.

Kupriyanova L, Alyoshina L. 1972. *Pollen and spores of plants from the flora of the European part of the USSR*, Leningrad (in Russian), Nauka.

Kupriyanova L, Alyoshina L. 1978. *Pollen and pores of plants from the flora of the European Part of the USSR*, Leningrad (in Russian).

Larocque I. 2001. How many chironomid head capsules are enough? A statistical approach to determine sample size for palaeoclimatic reconstructions. *Palaeogeography, Palaeoclimatology, Palaeoecology* **172**: 133–142.

Laskar J, Robutel P, Joutel F et al. 2004. A long-term numerical solution for the insolation quantities of the Earth. *Astronomy & Astrophysics* **428**: 261–285.

Last W, Smol J. 2001. *Tracking environmental change using lake sediments. Physical and geochemical methods.* Springer: Dordrecht.

Leemann A, Niessen F. 1994. Holocene glacial activity and climatic variations in the Swiss Alps: reconstructing a continuous record from proglacial lake sediments. *The Holocene* **4**: 259–268.

Leonard EM. 1986. Varve Studies at Hector Lake, Alberta, Canada, and the Relationship between Glacial Activity and Sedimentation. *Quaternary Research* **25**: 199–214.

Lisiecki LE, Raymo ME. 2005. A Plio-Pleistocene stack of 57 globally distributed benthic $\delta^{18}O$ records. *Paleoceanography* **20**: 1–17.

Lohne ØS, Mangerud JAN, Birks HH. 2014. IntCal13 calibrated ages of the Vedde and Saksunarvatn ashes and the Younger Dryas boundaries from Kråkenes, western Norway. *Journal of Quaternary Science* **29**: 506–507.

Mangerud J, Jakobsson M, Alexanderson H et al. 2004. Ice-dammed lakes and rerouting of the drainage of northern Eurasia during the Last Glaciation. *Quaternary Science Reviews* **23**: 1313–1332.

Mangerud J, Gosse J, Matiouchkovc A et al. 2008. Glaciers in the Polar Urals, Russia, were not much larger during the Last Global Glacial Maximum than today. *Quaternary Science Reviews* **27**: 1047–1057.

Melles M, Brigham-Grette J, Glushkova OY et al. 2007. Sedimentary geochemistry of core PG1351 from Lake El'gygytgyn - a sensitive record of climate variability in the East Siberian Arctic during the past three glacial-interglacial cycles. *Journal of Paleolimnology* **37**: 89–104.

Meyers PA. 1997. Organic geochemical proxies of paleoceanographic, paleolimnologic, and paleoclimatic processes. *Organic Geochemistry* **27**: 213–250.

Meyers PA. 2003. Applications of organic geochemistry to paleolim-nological reconstructions: a summary of examples from the Laurentian Great Lakes. *Organic Geochemistry* **34**: 261–289.

Meyers PA, Ishiwatari R. 1993. Lacustrine organic geochemistry—an overview of indicators of organic matter sources and diagenesis in lake sediments. *Organic geochemistry* **20**: 867–900.

Meyers PA, Teranes JL. 2001. Sediment Organic Matter. In *Tracking environmental change using lake sediments. Physical and geochemical methods*, Last WM, Smol JP (eds). Springer: Dordrecht.239–270.

Miller GH, Brigham-Grette J, Alley RB *et al.* 2010. Temperature and precipitation history of the Arctic. *Quaternary Science Reviews* **29**: 1679–1715.

Moller Pillot HKM. 2009. Chironomidae Larvae. *Chironomini: Biology and Ecology of the Chironomini, KNNV Publishing* **2**.

Mortlock RA, Froelich PN. 1989. A simple method for the rapid determination of biogenic opal in pelagic marine sediments. *Deep Sea Research Part A. Oceanographic Research Papers 36* 1415–1426.

Müller PJ, Schneider R. 1993. An automated leaching method for the determination of opal in sediments and particulate matter. *Deep Sea Research Part I: Oceanographic Research Papers* **40**: 425–444.

Murray AS, Wintle AG. 2003. The single aliquot regenerative dose protocol: potential for improvements in reliability. *Radiation measurements* **37**: 377–381.

Nazarova L, Pestryakova L, Ushnitskaya LA *et al.* 2008. Chironomids (Diptera: Chironomidae) in lakes of central Yakutia and their indicative potential for paleoclimatic research. *Contemporary Problems of Ecology* **1**: 335–345.

Nazarova L, Herzschuh U, Wetterich S *et al.* 2011. Chironomid-based inference models for estimating mean July air temperature and water depth from lakes in Yakutia, northeastern Russia. *Journal of Paleolimnology* **45**: 57–71.

Nazarova L, Self AE, Brooks SJ *et al.* 2015a. Northern Russian chironomid-based modern summer temperature data set and inference models. *Global and Planetary Change* **134**: 10–25.

Nazarova LB, Sapelko TV, Kuznetsov DD *et al.* 2015b. Palaeoecolo-gical and palaeoclimatical reconstructions of Holocene according chironomid analysis of Lake Glubokoye sediments. *Doklady Biological Sciences* **460**: 57–60.

Nazarova L, Bleibtreu A, Hoff U *et al.* 2017a. Changes in temperature and water depth of a small mountain lake during the past 3000 years in Central Kamchatka reflected by a chironomid record. *Quaternary International* **447**: 46–58.

Nazarova L, Self AE, Brooks SJ *et al.* 2017b. Chironomid fauna of the lakes from the Pechora river basin (east of European part of Russian Arctic): Ecology and reconstruction of recent ecological changes in the region. *Contemporary Problems of Ecology* **10**: 350–362.

Nazarova LB, Subetto DA, Syrykh LS *et al.* 2018. Reconstructions of Paleoecological and Paleoclimatic Conditions of the Late Pleisto-cene and Holocene according to the Results of Chironomid Analysis of Sediments from Medvedevskoe Lake (Karelian Isthmus). *Doklady Earth Sciences* **480**: 710–714.

Nazarova L, Syrykh LS, Mayfield RJ *et al.* 2020. Palaeoecological and palaeoclimatic conditions on the Karelian Isthmus (northwestern Russia) during the Holocene. *Quaternary Research* **95**: 65–83.

Néel L. 1955. Some theoretical aspects of rock-magnetism. *Advances in Physics* **4**: 191–243.

New M, Lister D, Hulme M *et al.* 2002. A high-resolution data set of surface climate over global land areas (accessed 05.05.2020). *Climate Research* **21**: 1–25.

Nowaczyk NR, Melles M, Minyuk P. 2007. A revised age model for core PG1351 from Lake El'gygytgyn, Chukotka, based on magnetic susceptibility variations tuned to northern hemisphere insolation variations. *Journal of Paleolimnology* **37**: 65–76.

Palagushkina O, Wetterich S, Biskaborn BK *et al.* 2017. Diatom records and tephra mineralogy in pingo deposits of Seward Peninsula, Alaska. *Palaeogeography, Palaeoclimatology, Palaeoe-cology* **479**: 1–15.

Paus A, Svendsen JI, Matiouchkov A. 2003. Late Weichselian (Valdaian) and Holocene vegetation and environmental history of the northern Timan Ridge, European Arctic Russia. *Quaternary Science Reviews* **22**: 2285–2302.

Plikk A, Engels S, Luoto TP *et al.* 2019. Chironomid-based temperature reconstruction for the Eemian Interglacial (MIS 5e) at Sokli, northeast Finland. *Journal of Paleolimnology* **61**: 355–371.

Puchkov VN. 1997. Structure and geodynamics of the Uralian orogen. *Geological Society London Special Publications* **121**: 201–236.

Quinlan R, Smol JP. 2001. Setting minimum head capsule abundance and taxa deletion criteria in chironomid-based inference models. *Journal of Paleolimnology* **26**: 327–342.

R Core Team. 2020. A language and environment for statistical computing. R Foundation for Statistical Computing: Vienna, Austria.

Rasmussen SO, Andersen KK, Svensson AM *et al.* 2006. A new Greenland ice core chronology for the last glacial termination. *Journal of Geophysical Research: Atmospheres* **111**: 1–16.

Regnéll C, Haflidason H, Mangerud J *et al.* 2019. Glacial and climate history of the last 24 000 years in the Polar Ural Mountains, Arctic Russia, inferred from partly varved lake sediments. *Boreas* **48**: 432–443.

Reille M. 1992. *Pollen et Spores d'Europe et d'Afrique du nord*, Marseille [in French], Laboratoire de Botanique Historique et Palynologie.

Reille M. 1995. *Pollen et spores d'Europe et d'Afrique du Nord: Supplément 1. Laboratoire de Botanique Historique et Palynologie*, Marseille [in French], Laboratoire de Botanique Historique et Palynologie.

Reille M. 1998. *Pollen et spores d'Europe et d'Afrique du Nord, Supplément 2, Laboratoire de Botanique Historique et Palynologie*, Marseille [in French], Laboratoire de Botanique Historique et Palynologie.

Reilly BT, Stoner JS, Hatfield RG *et al.* 2018. Regionally consistent Western North America paleomagnetic directions from 15 to 35 ka: Assessing chronology and uncertainty with paleosecular variation (PSV) stratigraphy. *Quaternary Science Reviews* **201**: 186–205.

Reimer PJ, Austin WEN, Bard E *et al.* 2020. The IntCal20 Northern Hemisphere. *Radiocarbon Age Calibration Curve (0–55 cal kbp). Radiocarbon* **62**: 725–757.

Rethemeyer J, Fülöp RH, Höfle S *et al.* 2013. Status report on sample preparation facilities for ^{14}C analysis at the new CologneAMS center. *Nuclear Instruments and Methods in Physics Research Section B: Beam Interactions with Materials and Atoms* **294**: 168–172.

Roberts AP, Hu P, Harrison RJ *et al.* 2019. Domain state diagnosis in rock magnetism: evaluation of potential alternatives to the Day diagram. *Journal of Geophysical Research: Solid Earth* **124**: 5286–5314.

Rolf C. 2000. Das Kryogenmagnetometer im Magnetiklabor Gruben-hagen. *Geologisches Jahrbuch* **52**: 161–188 (in German).

Scheidt S, Egli R, Frederichs T *et al.* 2017. A mineral magnetic characterization of the Plio-Pleistocene fluvial infill of the Heidel-berg Basin (Germany). *Geophysical Journal International* **210**: 743–764.

Seierstad IK, Abbott PM, Bigler M *et al.* 2014. Consistently dated records from the Greenland GRIP, GISP2 and NGRIP ice cores for the past 104 ka reveal regional millennial-scale δ18O gradients with possible Heinrich event imprint. *Quaternary Science Reviews* **106**: 29–46.

Singer BS, Jicha BR, He H *et al.* 2014. Geomagnetic field excursion recorded 17 ka at Tianchi Volcano, China: New 40Ar/39Ar age and significance. *Geophysical Research Letters* **41**: 2794–2802.

Solomina O, Bradley RS, Hodgson DA *et al.* 2015. Holocene glacier fluctuations. *Quaternary Science Reviews* **111**: 9–34.

Solomina O, Ivanov M, Bradwell T. 2010. Lichenometric studies on moraines in the polar urals. *Geografiska Annaler: Series A. Physical Geography* **92**: 81–99.

Solomina O, Bradley RS, Jomelli V *et al.* 2016. Glacier fluctuations during the past 2000 years. *Quaternary Science Reviews* **149**(61): 90.

Solovieva N, Klimaschewski A, Self AE *et al.* 2015. The Holocene environmental history of a small coastal lake on the north-eastern Kamchatka Peninsula. *Global and Planetary Change* **134**: 55–66.

Steinhart M. 2000. The life cycle of Hydrobaenus lugubris Fries, 1830, a chironomid (Diptera) species dwelling in temporary waters. *SIL Proceedings, 1922-2010* **27**: 2392–2395.

Stockmarr J. 1971. Tablets with spores used in absolute pollen analysis. *Pollen et Spores* **13**: 615–621.

Svendsen JI, Alexanderson H, Astakhov VI *et al*. 2004. Late Quaternary ice sheet history of northern Eurasia. *Quaternary Science Reviews* **23**: 1229–1271.

Svendsen JI, Kruger LC, Mangerud J *et al*. 2014. Glacial and vegetation history of the Polar Ural Mountains in northern Russia during the Last Ice Age, Marine Isotope Stages 5-2. *Quaternary Science Reviews* **92**: 409–428.

Svendsen JI, Færseth LMB, Gyllencreutz R *et al*. 2019. Glacial and environmental changes over the last 60 000 years in the Polar Ural Mountains, Arctic Russia, inferred from a high-resolution lake record and other observations from adjacent areas. *Boreas* **48**: 407–431.

Swann G, Mackay A. 2006. Potential limitations of biogenic silica as an indicator of abrupt climate change in Lake Baikal, Russia. *Journal of Paleolimnology* **36**: 81–89.

Syrykh LS, Nazarova LB, Herzschuh U *et al*. 2017. Reconstruction of palaeoecological and palaeoclimatic conditions of the Holocene in the south of the Taimyr according to an analysis of lake sediments. *Contemporary Problems of Ecology* **10**: 363–369.

Tarasov P, Peyron O, Guiot J *et al*. 1999. Last Glacial Maximum climate of the former Soviet Union and Mongolia reconstructed from pollen and plant macrofossil data. *Climate Dynamics* **15**: 227–240.

Tauxe L, Bertram HN, Seberino C. 2002. Physical interpretation of hysteresis loops: Micromagnetic modeling of fine particle magnetite. *Geochemistry, Geophysics, Geosystems* **3**: 1055.

Thomsen KJ, Murray AS, Jain M *et al*. 2008. Laboratory fading rates of various luminescence signals from feldspar-rich sediment extracts. *Radiation measurements* **43**: 1474–1486.

Turney CSM. 1999. Lacustrine Bulk Organic δ13C in the British Isles during the Last Glacial-Holocene Transition (14-9 ka ^{14}C bp). *Arctic, Antarctic, and Alpine Research* **31**: 71–81.

Van der Bilt WGM, Bakke J, Vasskog K *et al*. 2016. Glacier-fed lakes as palaeoenvironmental archives. *Geology Today* **32**: 213–218.

Van Geel B. 2002. Non-pollen palynomorphs. In *Tracking environmental change using lake sediments. Terrestrial, Algal, and Siliceous Indicators*, Smol JP, Birks JB, Last WM (eds). Springer: Dordrecht.99–119.

Wagner B, Cremer H. 2006. Limnology and sedimentary record of Radok Lake, Amery Oasis, East Antarctica. In *Antarctica: contributions to global earth sciences*, Fütterer DK, Damaske D, Kleinschmidt G *et al*. (eds). Springer-Verlag: Berlin Heidelberg New York.45–54.

Wetterich S, Schirrmeister L, Nazarova L *et al*. 2018. Holocene thermokarst and pingo development in the Kolyma Lowland (NE Siberia). *Permafrost and Periglacial Processes* **29**(182): 198.

Wiederholm T. 1983. *Chironomidae of the Holarctic region. Keys and diagnoses. Part I. Larvae*, Entomologica Scandinavica.

Wood R. 2015. From revolution to convention: the past, present and future of radiocarbon dating. *Journal of Archaeological Science* **56**: 61–72.

Zander A, Hilgers A. 2013. Potential and limits of OSL, TT-OSL, IRSL and pIRIR 290 dating methods applied on a Middle Pleistocene sediment record of Lake El'gygytgyn, Russia. *Climate of the Past* **9**: 719–733.